Facile Tri-Metallic Catalyst Fabrication Using the Dynamic Hydrogen Bubble Template method

Carlos M. S. Lobo, Bruna F. Gomes, Lu Xia, Wulyu Jiang, Tengyu Chen, Kaiqi Zhao, Laís G. Vernasqui, Hannah Kammal, Eric Liesz, Jonas Prietz, F. Pelayo García de Arquer, and Christina Roth*

Electrocatalysts play a fundamental role in enabling and enhancing the efficiency of a variety of energy-transition-relevant reactions (e.g. water electrolysis, fuel cells, and CO_2 conversion to value-added products). Multi-elemental electrocatalysts are particularly attractive because they often outperform their mono- or bi-metallic counterparts. However, the design and fabrication of such catalysts with high surface area remains challenging due to limitations in synthetic control and compositional complexity. Here, the Dynamic Hydrogen Bubble Template (DHBT) method is used—a facile approach to fabricate freestanding, binder-free metallic foams with hierarchical porosity—to synthesize Ni-based mono-, bi-, and tri-metallic electrocatalysts. The materials are subsequently annealed and evaluated for two model reactions: oxygen evolution and glucose oxidation. Annealing enhances both crystallinity and electrochemically active surface area (ECSA), likely due to Mn surface segregation and nanocrystallization at grain boundaries. Among the compositions, NiMn exhibits the highest post-anneali mass-normalized ECSA (36 $m^2\ g_{cat}^{-1}$), although this does not translate into improved catalytic activity. In contrast, NiMn and NiMnFe achieve the highest mass-specific activities, followed by NiFeMo. Anion Exchange Membrane Water Electrolysis tests (AEMWE) showed that NiMnFe achieved over 3.4 A cm^{-2} at 2.0 V in alkaline conditions. This study demonstrates that DHBT is a viable and versatile method for fabricating multimetallic electrocatalysts with tunable porosity and composition, enabling the controlled synthesis of porous multi-metallic structures and offering a promising route toward high-entropy alloy formation through electrolyte composition tuning and annealing procedures.

1. Introduction

Electrocatalysts play a fundamental role in enhancing the efficiency of several reactions relevant to the energy transition (such as water electrolysis, fuel cells, CO_2 conversion to value-added products). By reducing activation energy and increasing reaction rates electrocatalysts enable more sustainable and scalable energy technologies. Their performance is strongly affected by their surface area, as a larger active surface provides more sites for reactant interactions.[1] In particular, multi-elemental catalysts have gained increasing attention in recent years due to their potential to surpass the limitations of traditional mono- and bi-metallic systems. By carefully selecting and combining different elements, it is possible to develop catalysts with enhanced activity, stability, and selectivity, making them promising candidates for applications in energy conversion, environmental remediation, and industrial catalysis.[2–5]

One key reason for the improved performance of multi-elemental electrocatalysts lies in synergistic effects arising from element–element interactions. These effects can manifest as: (i) electronic modifications, where the presence of

---

C. M. S. Lobo, B. F. Gomes, H. Kammal, E. Liesz, J. Prietz, C. Roth
Chair of Electrochemical Process Engineering
Faculty of Engineering
University of Bayreuth
95447 Bayreuth, Germany
E-mail: carlos.lobo@uni-bayreuth.de

L. Xia, W. Jiang, T. Chen, K. Zhao, F. P. García de Arquer
Institut de Ciències Fotòniques
The Barcelona Institute of Science and Technology
Castelldefels 08860, Barcelona, Spain

L. G. Vernasqui
National Institute for Space Research - INPE
São José dos Campos 12227-010, Brazil

The ORCID identification number(s) for the author(s) of this article can be found under https://doi.org/10.1002/adfm.202509522

DOI: 10.1002/adfm.202509522

Table 1. Summary of tri-metallic catalyst fabrication methods found in the literature, including examples and advantages and disadvantages of each method.

Fabrication method	Catalyst example	Ref.	Advantage(s)	Disadvantage(s)	Refs.
Impregnation	FeNiCe nanoparticles	[12]	Simple and cheap	Limited or lack of size control, poor metal alloying, difficult to control sufrace composition, nanoparticles/agglomerates	[13]
Chemical Vapor Deposition (CVD)	FeNiVOx[a]	[14]	Uniform, high-purity, stable films	Thin (non-porous) films, highly expensive instrumentation, emits toxic by-products	[15]
Physical Vapor Deposition (PVD)	FeRhAu	[16]	Appropriate for inorganic and some organic materials, environmentally friendly	Thin (non-porous) films, complex shapes can't be coated properly, high cost, complex process	[17]
Sol-gel	Fe_2O_3-MgO-CuO	[18]	Good control of particle structure and size, porous samples	Contamination by reaction products, post treatment required	[19]
Hydrothermal treatment	NiFeMo for water splitting	[20]	Low-cost instrumentation, high-yield, high-quality, environmentally friendly, nanomaterial size and morphology control	Performed at high T and P, challenges with scaling up, reactor blockages caused by poor mixing	[15]

[a] Using aerosol-assisted CVD

additional elements alters the electronic structure of active sites, optimizing adsorption/desorption energetics;[2] (ii) geometric effects, such as lattice strain or altered coordination environments;[3] and (iii) improved stability and resistance to deactivation due to reduced sintering and poisoning, leading to longer catalyst lifetimes.[4] For instance, in hydrogen evolution and oxygen reduction reactions, tri-metallic electrocatalysts such as Pt-Ni-Co outperform monometallic Pt due to optimized electronic structure and synergistic interactions.[6,7]

Building on these concepts, high entropy alloys (HEAs)—typically comprising five or more elements in near-equimolar ratios—have emerged as a new class of catalysts. Their high configurational entropy stabilizes single-phase solid solutions and provides a large distribution of potential active sites, contributing to enhanced catalytic activity, robustness, and compositional flexibility.[8–10] These properties make HEAs highly promising for complex reactions such as the oxygen evolution reaction (OER) and oxygen reduction reaction (ORR).

Despite their promise, designing and fabricating multi-elemental catalysts with a high surface area remains challenging. Many synthesis strategies offer limited compositional/morphological control[11] or require complex instrumentation, such as vacuum deposition or high-energy ball milling, while others rely on wet-chemistry approaches with varying reproducibility. These factors complicate the scalable production of multi-metallic catalysts, particularly those intended for porous, high-surface-area morphologies (see **Table 1**).

The Dynamic Hydrogen Bubble Template (DHBT) method has emerged as a promising approach for fabricating freestanding, binder-free metallic foams with hierarchical porous structure. DHBT leverages in-situ hydrogen evolution during metal electrodeposition, where evolving H_2 bubbles act as dynamic templates. Rather than hindering the process, as in conventional electrodeposition,[21] the bubbles locally block deposition, forcing metal ions to deposit around them. As bubbles grow, coalesce, and detach, they generate a complex porous architecture (**Figure 1**). Crucially, DHBT offers tunability of pore size and morphology through parameters such as current density, deposition time, pH gradients, stirring rate, and electrolyte composition (e.g., use of acids or NH_4Cl).[22] These factors make DHBT an attractive, simple, and scalable option for tailoring catalytic foams across a wide range of compositions and morphologies.

In this study, we explore the use of DHBT to fabricate Ni-based bi-, and tri-metallic foams onto Ni and carbon substrates. Importantly, DHBT allows the co-deposition of multiple elements, facilitating the exploration of synergistic effects in multi-elemental systems while maintaining structural control. Additionally, the electrochemical performance of the fabricated foams was evaluated toward two model reactions: the OER and the glucose oxidation reaction (GOR), since Ni is known to be active toward GOR and OER making it a suitable base metal for compositional extension with Mn, Co, Mo, and Fe—transition metals that are redox-active and widely used in electrocatalysis.[23–25] These combinations were selected to balance thermodynamic compatibility and potential synergistic effects.

Thanks to their high surface area and interconnected porosity, we expect the DHBT-derived foams to support high current densities. Moreover, their pore geometries may promote localized micro-environments that influence mass transport,

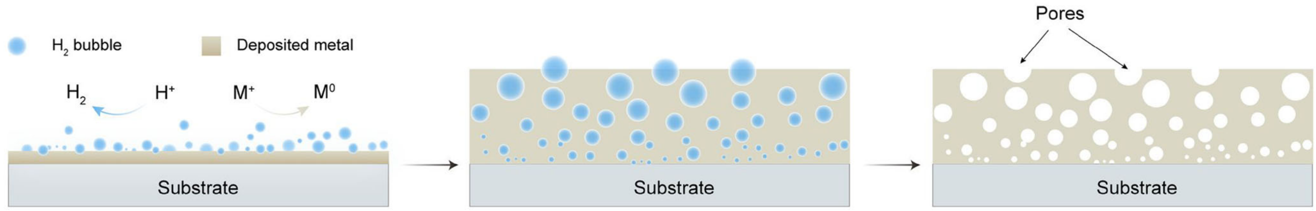

Figure 1. The simplified DHBT process.

intermediate stabilization, or reaction pathways—possibly enhancing selectivity.[26,27]

While the use of bubbles as templates dates back decades, our approach advances the field by linking the DHBT fabrication method, structural analysis, and catalytic performance. By combining synchrotron-based structural characterization with electrochemical testing and scalable fabrication strategies, this study contributes to a deeper understanding of structure–activity–manufacturability relationships, addressing both fundamental and practical aspects of catalyst development.

Annealing procedures were tested to limit oxidation of the samples after fabrication and to assess its suitability in enhancing activity of the electrocatalysts. This was done because annealing treatments are widely used in metallurgy and catalytic materials engineering to relieve lattice strain, reduce crystallographic defects, and promote atomic ordering by recovery, recrystallization, and grain growth mechanisms.[28] In multimetallic samples, especially those generated via non-equilibrium methods like DHBT electrodeposition, thermal diffusion during annealing can drive selective surface segregation, often enriching more oxophilic or lower–surface-energy elements at the surface—an effect strongly influenced by the annealing atmosphere.[29–32] Such redistribution alters both the structural and electronic properties of the catalyst surface, with direct consequences for electrocatalytic activity and long-term stability.[30,32]

Altogether, this work highlights DHBT as a scalable and robust platform for the synthesis of multimetallic electrocatalysts, demonstrating its viability for fabricating complex, high-surface-area foams with compositional flexibility.

2. Results and Discussion

2.1. Considerations Regarding DHBT

According to René Winand,[33] metals can be classified into three groups: *i*) normal metals (such as Cd, Zn, Sn, Ag) which have a low melting point and high exchange current density ($j_0 \geqslant 1$ A dm^{-2}); *ii*) intermediate metals (such as Au and Cu) which have a moderate melting point and medium exchange current density (10^{-2} A dm$^{-2} \leqslant j_0 \leqslant 1$ A dm^{-2}); and *iii*) inert metals (such as Fe, Ni, Co, Pt, Cr, and Mn) which have a high melting point and low exchange current density ($j_0 \leqslant 10^{-2}$ A dm^{-2}).

It was previously thought that not all metals could be deposited as a 3D foam,[34] particularly the inert metals. However, not long ago Popov et al. demonstrated that the DHBT method can indeed be used with metals from all three of Winand's classification groups[35] provided that sufficiently large bubbles are formed and the rate of metal deposition is comparable to the time that bubbles remain adsorbed on the substrate surface. As such, both the substrate and metal salt concentration play a crucial role in defining the 3D-structure of the foam (the metal salt can have a concentration ranging from 1 to 100 mmol L^{-1} or higher). Additionally, a source of H^+ ions is needed, which is usually NH_4Cl or other acids (with a concentration ranging from 0.1 to 2 mol L^{-1}). The use of surfactants and additives, such as ethylene glycol or sodium citrate, also critically affects bubble behavior by inhibiting bubble coalescence through reduced surface tension. Even at low concentrations, such additives can significantly impact the foam morphology.[36]

As one might imagine, there is a minimum current density that must be applied for the deposited metal to acquire a 3D structure, at least a few hundreds of mA cm^{-2} but usually a few A cm^{-2},[22,37–39] below which the hydrogen bubbles are not produced in sufficient quantity or stability to force the metal growth into a 3D structure. However, there is also a practical upper limit, since at excessively high current densities, hydrogen evolution becomes dominant and outcompetes metal deposition. In this regime, the electrode surface is rapidly covered by the large evolving H_2 bubbles,[40] which hinder electrolyte transport and suppress continuous metal ion reduction, ultimately leading to poor deposition quality.

Attempts at fabricating the foams for this study were initially made using the chloride salts of the metals. However, this quickly resulted in a dark substance forming at the surface of the solution over time, which is attributed to the metal ions oxidizing due to the higher pH in the vicinity of the electrode during the DHBT procedure. This issue was resolved by adding sodium citrate to the electrolyte, which immediately suppressed precipitate formation and facilitated post-deposition cleaning. The appearance of the insoluble substance in the solution occurred regardless of use of chlorides or sulfates, but sulfate salts were ultimately preferred, as they eliminate chlorine evolution, which is particularly detrimental for iron-containing foams due to rapid Fe oxidation in the presence of chloride. Therefore, the use of additives can be important not only because of their effect on the resulting porous structure, but also because they can help prevent the formation of insoluble byproducts that may contaminate the catalyst surface. This is especially relevant for metals like Mn, which readily form low-solubility oxides under alkaline or neutral pH conditions.

2.2. Foam Characterization

As previously mentioned, several metal combinations containing Ni have been tested, as well as the pure Ni foam. The tested mixtures were the following: NiMn, NiMnCo, NiMnFe, and NiFeMo. The following sections detail the physical characterization of the prepared samples.

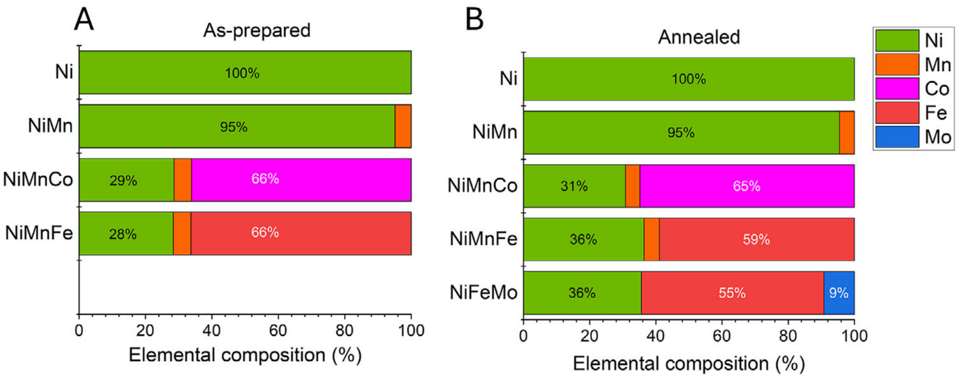

Figure 2. ICP-OES results of the as-prepared (A) and annealed (B) samples.

2.2.1. Morphology and Composition

Following the DHBT deposition, its success was checked using both ICP-OES and EDX. ICP-OES measurements confirmed that the desired elements were successfully deposited on the substrate. As can be seen in **Figure 2**, the as-prepared samples containing Mn exhibit 5% by mass of Mn, most likely due to the much more negative standard potential of the Mn reduction, as can be seen in **Table 2**. Similarly, samples with Mo contain around 10% of Mo by mass. Tri-metallic foams contain Ni at a consistent level of around 30%, while Co preferentially deposits in its foam, reaching 66% of the total deposited mass. In the NiMnFe foam, Fe accounts for 66% of the mass; however, when Mo is used instead of Mn, only 56% of Fe is deposited. Annealing does not significantly alter the resulting elemental composition. EDX (Figure S5, Supporting Information) analysis showed that the metals were homogeneously deposited throughout the foams.

The morphology of the foams was checked using SEM. As can be seen in **Figures 3** and **4**, the DHBT-fabricated foams are indeed porous. At a more macroscopic level (left-most images), all samples contain both circular and non-circular pores. However, the NiMn samples (Figures 3D–F and 4D–F) barely contain any circular pores and the majority of the deposited surface is covered with cracks. Since the pure Ni foam does not display this lack of circular pores, one possible explanation is that the Mn salt behaves as an additive which prevents bubbles from adsorbing on the electrode surface long enough for the metals to deposit around them, at least under the tested conditions. The presence of cracks on the deposited layer could be due to thermal stress. As described in the experimental section, active cooling is required during electrodeposition to prevent the substrate from overheating and fusing into the underlying steel support. Thus, the substrate temperature rises during the ON time, and quickly cools down during the OFF time, which could lead to cracks developing on the metal surface.

Table 2. Standard electrode potentials of the species involved in the DHBT depositions.

Reaction	$E^{\ominus}$ ($V_{\text{vs.NHE}}$)	Refs.
$Co^{2+} + 2e^{-} \longrightarrow Co(s)$	−0.277	[41]
$Ni^{2+} + 2e^{-} \longrightarrow Ni(s)$	−0.257	[41]
$Fe^{2+} + 2e^{-} \longrightarrow Fe(s)$	−0.440	[41]
$MoO_4^{2-} + 4H_2O + 6e^{-} \longrightarrow Mo(s) + 8OH^{-}$	−0.913	[42]
$Mn^{2+} + 2e^{-} \longrightarrow Mn(s)$	−1.180	[41]

The SEM images were used to determine the distribution of surface pore sizes (pores closer to the substrate are expected to be smaller—see Section S1, Supporting Information), with the exception of the NiMn samples which, as mentioned previously, barely contain any pores. As can be seen in **Figure 5**, the pore size distribution of all samples except the as-prepared NiMnFe follows a log-normal distribution. Interestingly, annealing reduces the median pore size – especially for the pure Ni foams, whose mean pore diameter decreases from 11.26 to 7.62 µm (Figure 5A).

In NiMnCo samples (Figure 5B) the median pore size appears to shift slightly to larger values after annealing, although not significantly. However, the mean pore size decreases marginally (from 7.55 to 7.05 µm). These minor changes, combined with relatively large standard deviations, likely reflect limitations in the measurement method rather than true structural differences. A similar observation applies to the NiMnFe samples (Figure 5C), which show a reduction in median pore size but a slight increase in mean size. Similar to the NiMnCo case, this is likely due to the pore estimation method, rather than an actual change in foam structure. Among all the fabricated foams, the annealed NiFeMo samples (Figure 5D) exhibit the smallest average pore diameter, with an average size of only 5.46 µm.

2.2.2. Crystal Structure

The crystal structure of the samples was evaluated using X-ray diffraction (XRD). As evidenced by the sharper reflections, the annealed samples exhibit significantly higher crystallinity. The crystal structure of the annealed pure Ni foam closely resembles the analyzed reference material (materials project mp-23), as the overall peak profile is preserved. However, since samples are porous, the XRD reflections do not retain the same position as those in the reference, as voids can cause local lattice distortions that lead to peak shifts. Indeed, the reflections are shifted toward lower 2θ values relative to the standard peaks, as shown in Table S1 (Supporting Information). Additionally, compared to

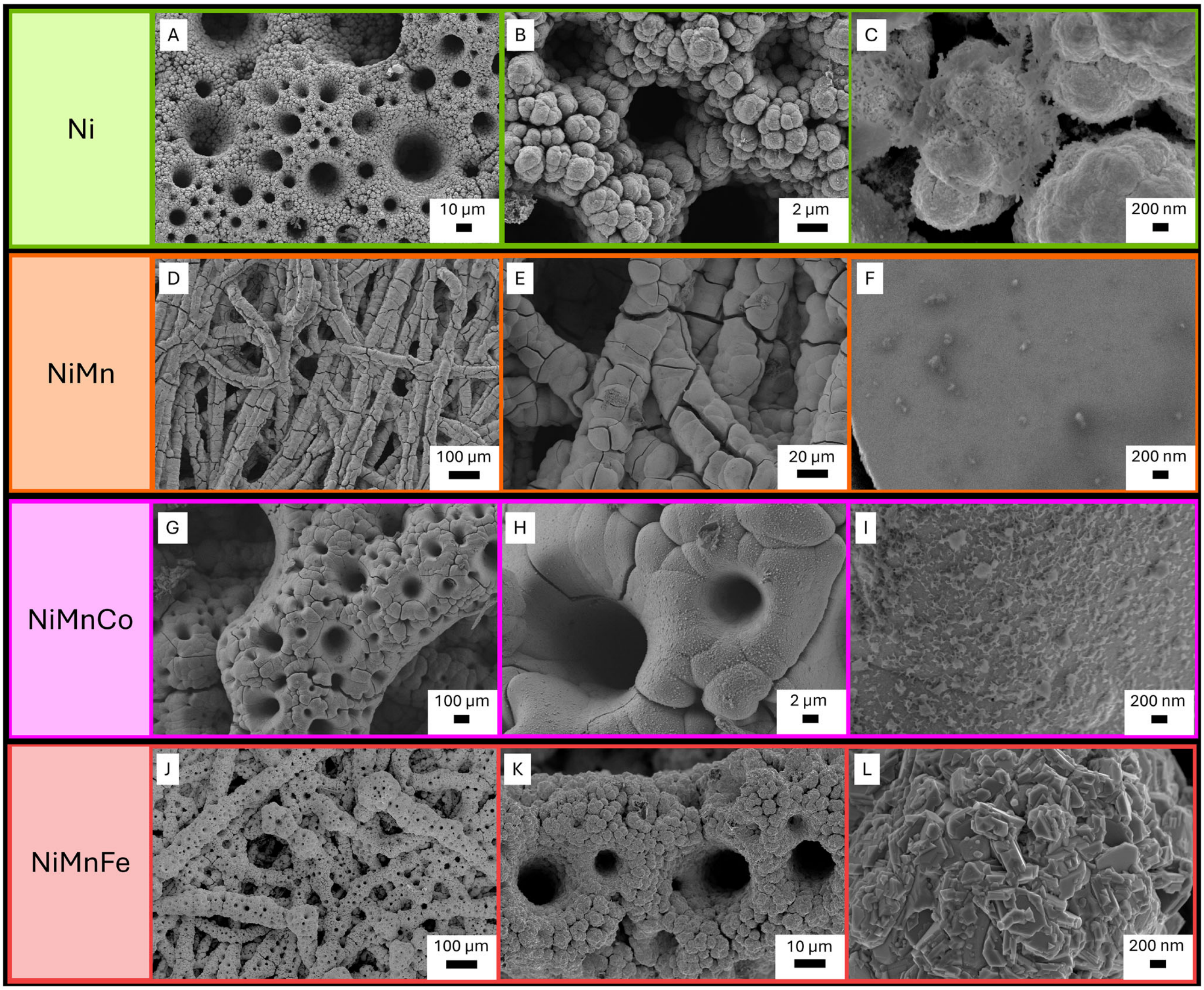

Figure 3. SEM images of as-prepared DHBT-fabricated foams. The foams were fabricated using pulsed deposition for a total of 20 min (total current ON time of 10 min). Ni foam (A–C), NiMn foam (D–F), NiMnCo (G–I), and NiMnFe (J–L).

the as-prepared samples, some reflections in the annealed foams shift slightly toward higher 2θ values, indicating a reduction in lattice parameters upon annealing (see inset in **Figure** 6A). Conversely, in post-mortem samples, some reflections shift back toward lower 2θ values, suggesting lattice expansion following electrochemical testing.

All samples show a reflection near 35° (although it is faint in the pure Ni sample) which is attributed to the (100) reflection of β-Ni(OH)$_2$.[43] Additional reflections for this phase would be expected at $2\theta = 20, 38, 40, 53, 59, 62, 69$, and 74 °, and most samples do seem to exhibit these features, although the porous nature of the samples again may lead to shifts in the reflections. Notably, the as-prepared NiMnFe sample lacks any of the higher-angle reflections, likely due to a combination of a preferred orientation low crystallinity/nanocrystalline domain size. The disappearance of the 35° reflection after annealing supports the hypothesis β-Ni(OH)$_2$ is a thermally labile phase.

An additional reflection of interest is observed at $2\theta \approx 28°$ for the NiMnFe and NiFeMo samples. As this feature disappears after annealing, it is assigned to the (103) plane of β-FeOOH,[44] which is expected to be removed by annealing in N_2 due to the elimination of surface-adsorbed oxygen.

Due to the porous nature of the samples, Scherrer analysis is not accurate as reflection broadening is dependent not only on the size (as assumed by the model) of the coherently scattering domains, but also on strain, defects, and porosity-induced internal stress. Williamson–Hall analysis was attempted on pure Ni foams to evaluate whether accounting for both crystallite size and strain could provide more structural information, but this approach did not provide meaningful results (see Section S2, Supporting Information). For the remaining samples, it is also evident that annealing increases crystallinity and that subsequent electrochemical testing did not significantly alter it.

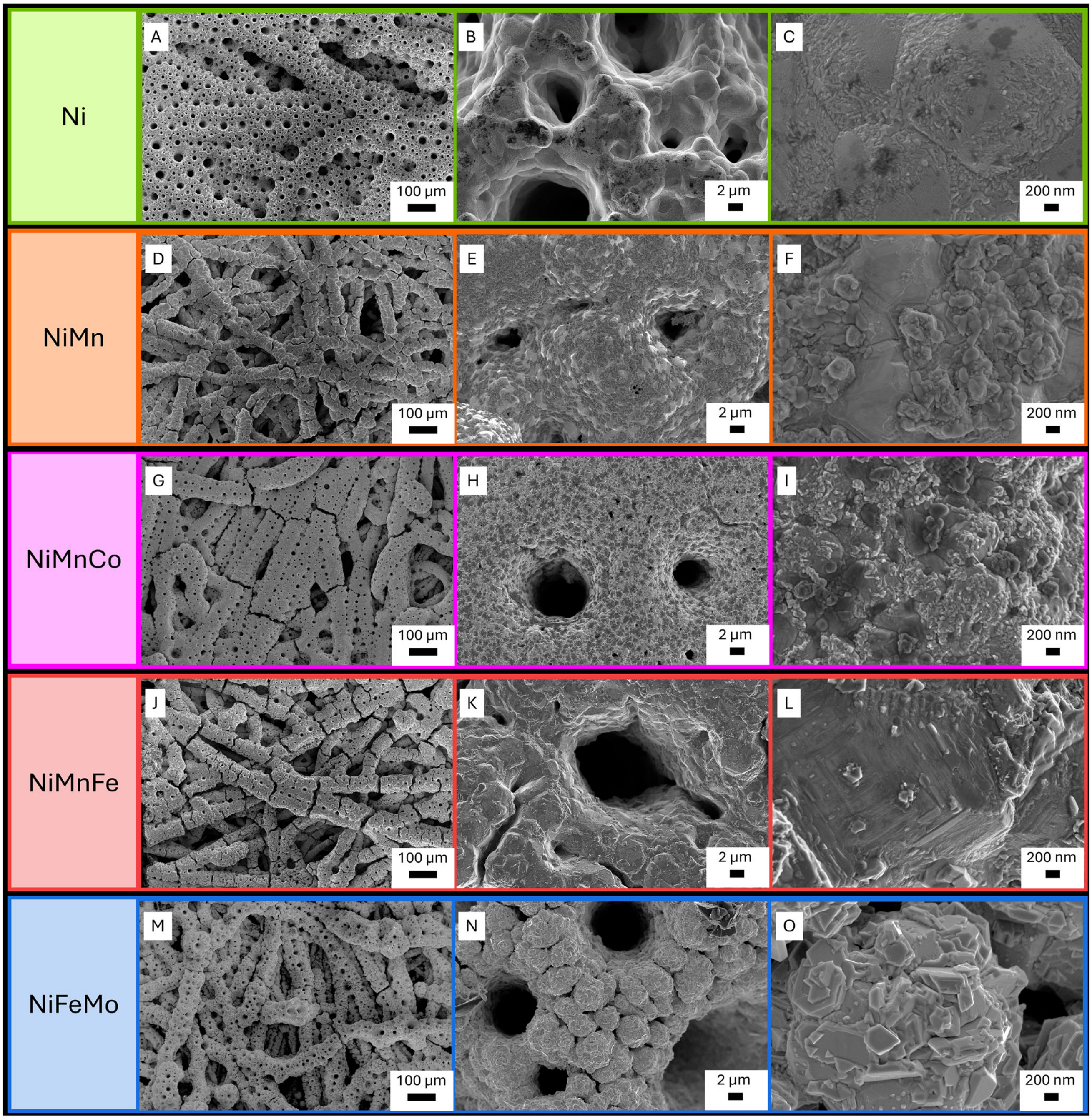

Figure 4. SEM images of annealed DHBT-fabricated foams. The foams were fabricated using pulsed deposition for a total of 20 min (total current ON time of 10 min). Ni foam (A–C), NiMn foam (D–F), NiMnCo (G–I), NiMnFe (J–L), and NiFeMo (M—O).

2.2.3. Bulk Properties

X-ray absorption spectroscopy (XAS) was used to investigate the bulk properties of the fabricated catalysts ex-situ. The XANES and FT-EXAFS results for the K-edges of Ni, Mn, Co, and Fe are summarized in **Figure 7**.

Looking first at the XANES data, we do not observe significant changes in the K-edges of Ni, Fe, and Co, but, in general, the absorption edge shifts slightly to lower energy either when the deposition time is increased or when annealing is applied. This implies that the elements exist in a slightly more reduced state upon annealing, which is consistent with annealing in a N_2 atmosphere: oxygen is removed from the surface, reducing the oxidation state of the metals. The bulk oxidation state also decreases with increasing deposition time. This trend can be attributed to a reduction in the surface-to-volume ratio: as thicker foams form, the surface contribution to the total XAS signal decreases, diminishing the contribution of more oxidized surface species.

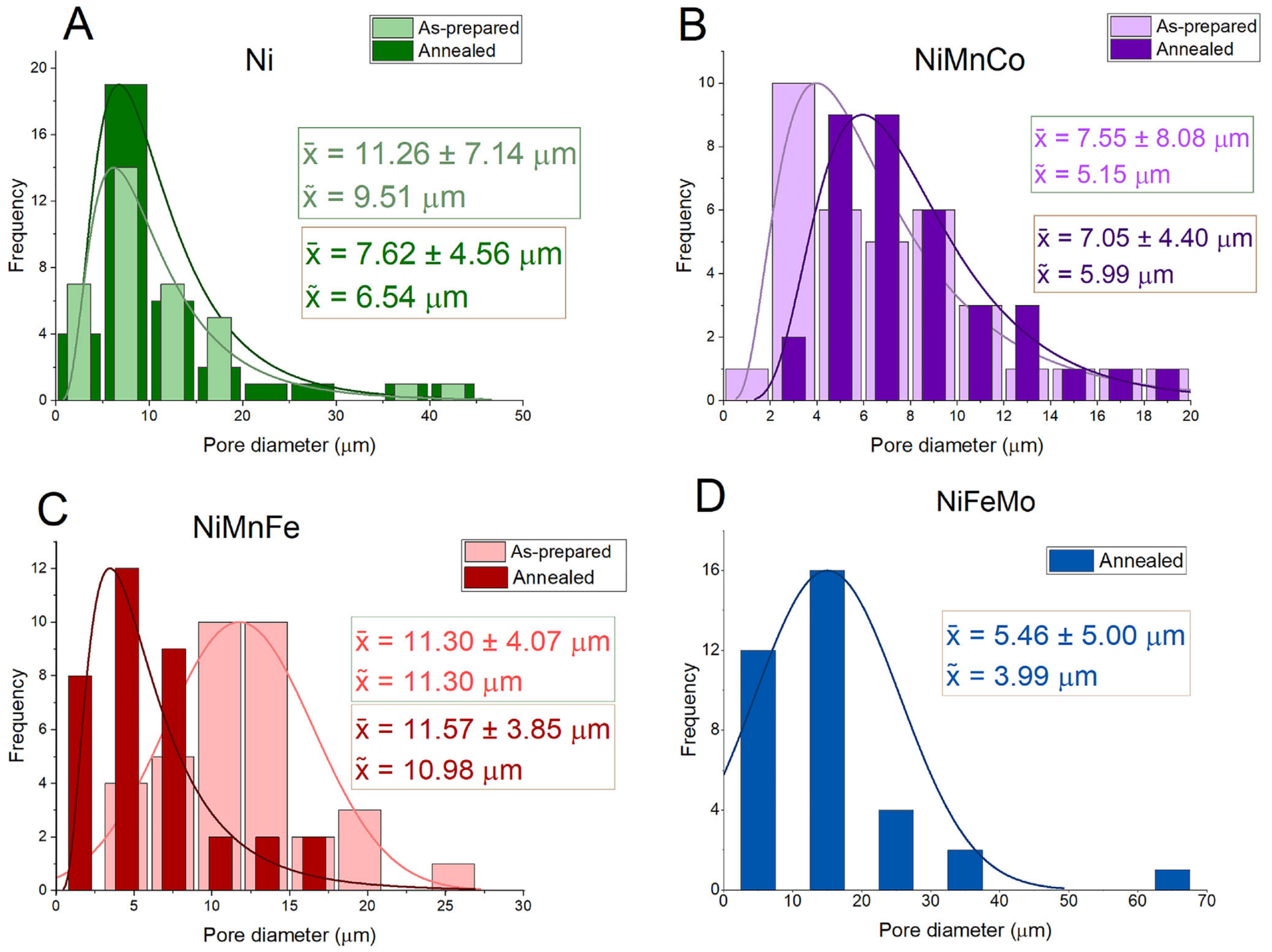

Figure 5. Surface pore size distribution histograms for the annealed and as-prepared (fresh) Ni (a), NiMnCo (b), NiMnFe (c), and NiFeMo (d). The best-fitting distribution function is also plotted over the histograms. $\bar{x}$ and $\tilde{x}$ represent the mean and median of each distribution, respectively.

FT-EXAFS for these same elements reveals that the annealing treatment introduces higher ordering in the samples: the intensity of the first-shell peak increases, and contributions from the second and third shells become more pronounced, supporting the XRD results. For the Ni foams, it was possible to reliably determine the coordination number around the Ni center (see Figures S9– S11, Supporting Information), and again observe an increase in crystallinity: the coodination number, N, increases after annealing, particularly at the fourth shell.

In contrast, the Mn K-edge shows substantial changes upon annealing. XANES spectra reveal that the white-line intensity increases significantly in all Mn-containing samples after annealing, indicating that Mn becomes more oxidized. This is further supported by the FT-EXAFS spectra, which show the clear emergence of a Mn-O first shell signal after annealing. Additionally, long-range order around Mn also improves, with peaks corresponding to the third Mn–M shell (M = Ni, Fe, or Co) appearing more clearly.

In the tri-metallic foams, increasing the deposition time of as-prepared samples reduces the oxidative character of Mn, as evidenced by a lower white line intensity. This suggests that Mn exists predominantly in the metallic state, with oxidation limited to surface atoms. Indeed, linear combination analysis of the XANES region of Mn-K edge spectra shows that all as-prepared samples contain at least around 30% Mn^0, while annealed samples contain only oxidized Mn species (Figure S1F, Supporting Information). This behavior supports the idea that, during annealing, larger atoms such as Mn migrate toward the surface due to size mismatch with the host lattice. This is consistent with Hume-Rothery's rules which state that solid solutions can form only if the involved elements have a size difference below 15%;[45] since Mn is around 10% larger than the surrounding elements, its segregation to the surface might be favored but not guaranteed. However, electrochemical factors and kinetic effects are likely dominant in this porous, non-equilibrium system.

2.2.4. Surface Properties

The surface of the prepared samples was characterized by both X-ray photoelectron spectroscopy (XPS) and Raman spectroscopy. XPS analysis (see **Table 3**; Figures S6 and S7, Supporting

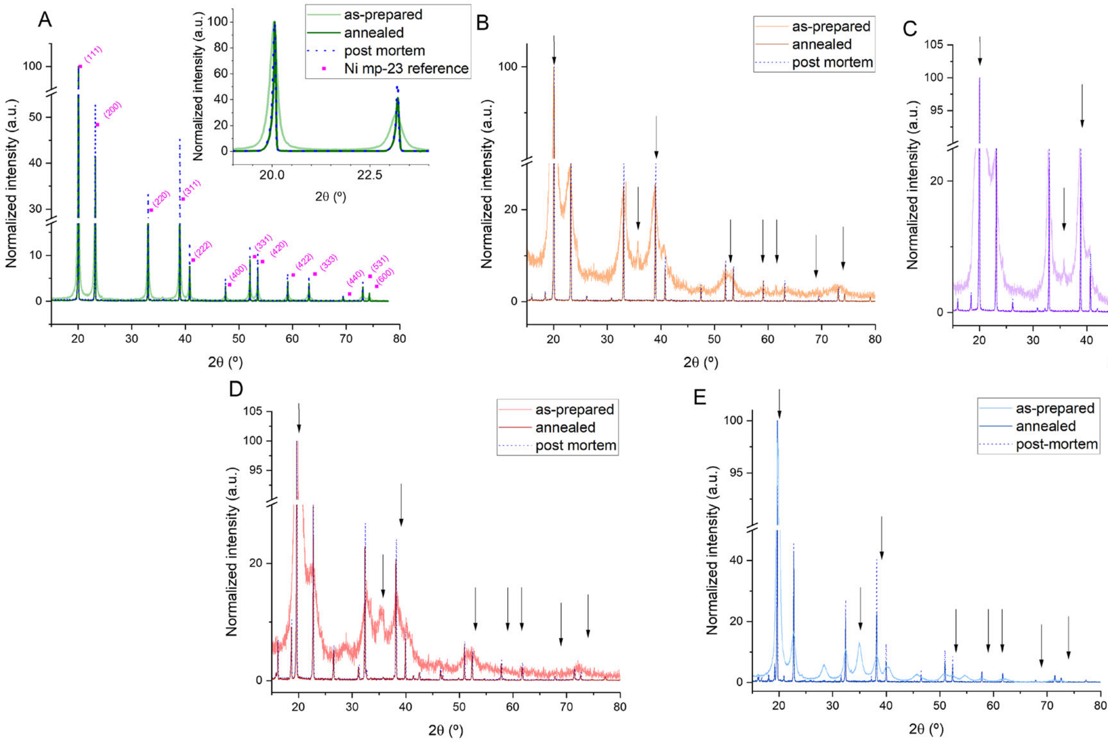

Figure 6. XRD patterns of the Ni (A), NiMn (B), NiMnCo (C), NiMnFe (D), and NiFeMo (E) foams. Black lines show the respective as-prepared foams, red lines show the annealed foams and the dotted blue lines show the post-mortem foams. The inset focuses on the two most intense reflections. The reference material shows only the position and relative intensity of its expected reflections. The arrows in panels B–E indicate the expected reflections of the β-Ni(OH)$_2$ phase.

Information) reveals that Mn is present in trace amounts at the surface prior to annealing, consistent with its relatively low mass loading. After annealing, the surface concentration of Mn increases in all Mn-containing samples: from 5% to 22% in NiMn, and up to 9.3% and 2.3% in NiMnCo and NiMnFe, respectively. This observation is consistent with the Mn K-edge XAS results, which indicate more oxidized Mn is present. XPS further reveals that Mn in the as-prepared samples is predominantly present as Mn^{2+}, with the exception of the NiMnCo sample, which shows a Mn^0 fraction exceeding 10%. After annealing, only oxidized species are detected, with Mn^{4+} reaching up to 50% in the NiMnFe sample. These results show strong agreement with the oxidation state distribution obtained via XAS XANES linear combination analysis discussed earlier. Surface concentrations of Mo, Co, and Fe also increase upon annealing, while Ni decreases in the NiMnCo sample but increases slightly in others.

Interestingly, O content increases in the Ni and NiMnFe samples, decreases in NiMnCo, and remains approximately constant in NiMn and NiFeMo. These variations may be related to differences in oxide formation, phase transformation, or surface restructuring during annealing, which can influence the effective thickness and composition of surface oxides. Annealing is also known to enhance the surface reactivity of certain materials toward O_2 due to defect formation and atomic rearrangement, which may contribute to the observed oxygen uptake in specific samples.[46]

The observed C signal is attributed to partial exposure of the underlying carbon substrate due to cracks or incomplete coverage in the metallic foam, as confirmed by SEM imaging. After annealing, the C signal decreases in most samples, likely due to thermal expansion and densification of the metallic network, which improves surface coverage and reduces the substrate contribution to the XPS signal.

Ex-situ Raman spectroscopy was also employed to monitor structural and compositional changes (**Figure 8**). In the as-prepared samples prepared using sulfates (NiMn, NiMnCo, and NiMnFe), a dominant and sharp band at ~990 cm^{-1} was observed, consistent with the ν_1 symmetric stretching vibration of surface-bound SO_4^{2-} species.[47] This feature was absent in the chloride-based Ni sample and disappeared after annealing in all sulfate-containing systems, confirming effective removal of surface sulfates. The strong signal from even trace SO_4^{2-} residues underscores the high sensitivity of Raman spectroscopy to synthesis byproducts. This observation suggests that refining the post-synthesis cleaning protocol could further improve sample purity.

Beyond sulfate removal, Raman spectroscopy reveals compositional and structural changes induced by annealing across the series of Ni-based metal systems. The Ni-only sample exhibited a broad signal centered around 500 cm^{-1} in the as-prepared state, likely due to the presence of a thin, disordered NiO_x layer. After annealing, the spectrum showed a marked decrease in intensity, with only a very broad and faint signal near 300 cm^{-1}, suggesting reduction or reorganization of surface oxides into a Raman-inactive or more compact phase.

In NiMn and NiMnCo, weak M—O signals in the as-prepared state developed into broader features upon annealing. In the

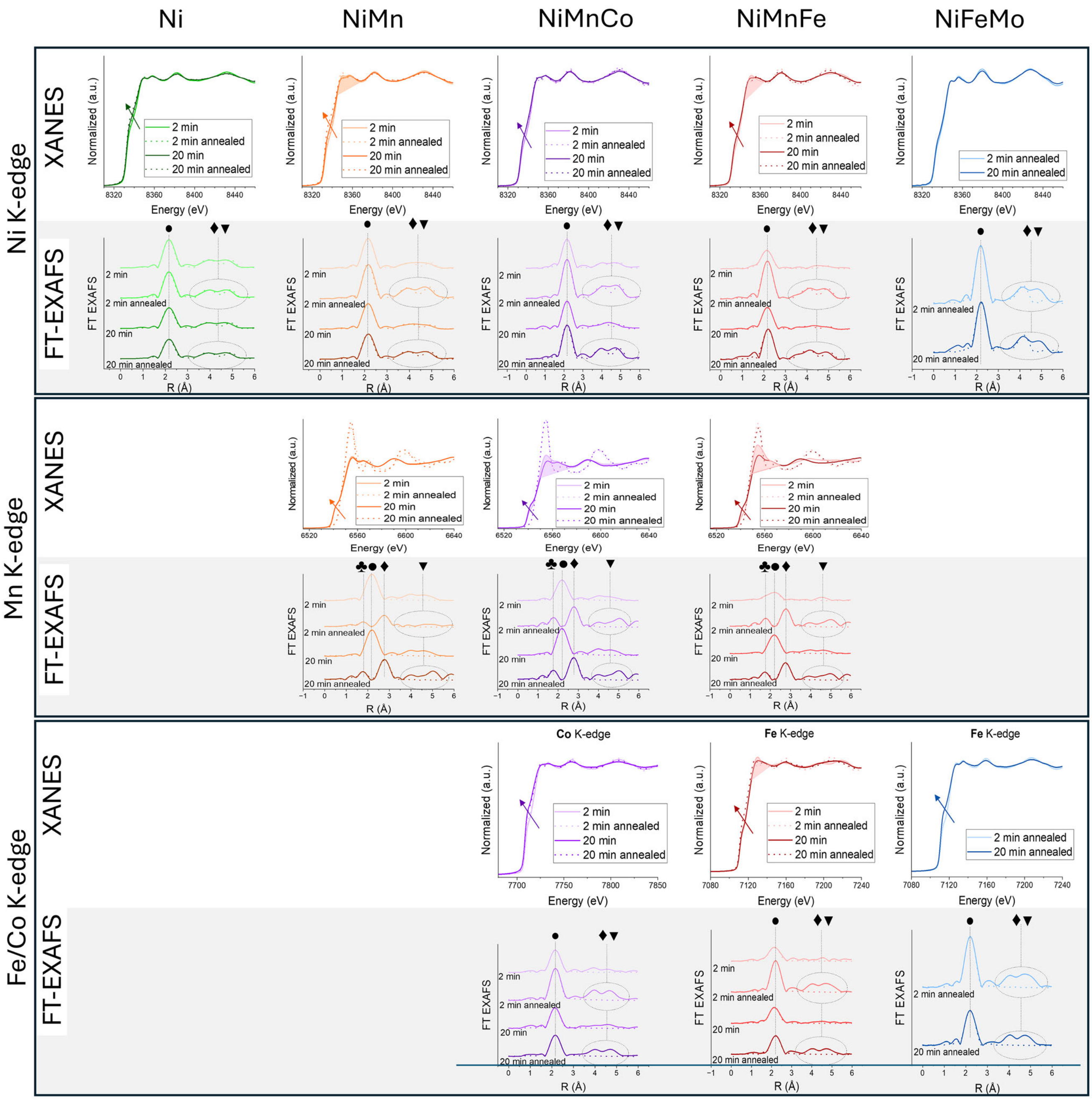

Figure 7. XAS results of the different samples (arranged column-wise) and for all the different measured edges. XANES (top row in each respective edge) and Fourier-Transform EXAFS (bottom row in each respective edge) data are shown. In the FT EXAFS rows the drawn symbols indicate M-M coordination (●); M-O-M coordination (♦); M-O-M coordination of more external shells (▼); M-O coordination (♣).

NiMn sample, the bands centered around 455 and 630 cm^{-1} shift to approximately 500 and 650 cm^{-1}, respectively, and are consistent with the formation of Ni—O and Mn—O bonding environments.[48,49] Additionally, the annealed NiMn sample exhibits a shoulder-like feature near 270 cm^{-1}, which may correspond to low-energy lattice vibrations or bending modes of M—O—M linkages,[50,51] possibly activated by increased local order or changes in symmetry.

In the NiMnCo sample, the as-prepared material showed multiple bands at around 290, 450, 630, 990, and 1140 cm^{-1}. The first band likely corresponds to stretching vibrations of Co—O,[52] while the bands at 450 and 630 cm^{-1} are attributed to Ni—O and Mn—O vibrations, respectively.[49] The two higher-frequency bands are assigned to the ν_1 and ν_3 modes of surface-bound sulfate.[53] Upon annealing, these sulfate-related bands disappear, and a broad band centered around 550–570 cm^{-1} emerges.

Table 3. Relative surface atomic composition of the samples (in %) resulting from XPS analysis.

Sample		O	C	Ni	Mn/Mo	Co/Fe
Ni	as prepared	52.78 ± 1.17	37.64 ± 0.13	9.58 ± 1.05	–	–
	annealed	68.72 ± 3.37	10.75 ± 0.45	20.54 ± 2.92	–	–
NiMn	as prepared	44.68 ± 1.09	45.89 ± 2.83	4.42 ± 1.30	5.02 ± 0.42	–
	annealed	44.95 ± 3.30	16.89 ± 0.00	13.45 ± 0.35	22.19 ± 0.00	–
NiMnCo	as prepared	52.77 ± 6.78	29.80 ± 0.69	12.30 ± 0.40	7.34 ± 0.13	2.80 ± 0.47
	annealed	49.07 ± 4.15	18.29 ± 6.71	0.91 ± 0.76	9.38 ± 1.12	22.36 ± 0.70
NiMnFe	as prepared	35.50 ± 30.65	66.36 ± 27.73	0.12 ± 0.08	0.25 ± 0.29	0.29 ± 0.23
	annealed	50.86 ± 1.04	21.61 ± 1.58	1.80 ± 1.87	2.31 ± 0.30	23.44 ± 2.11
NiFeMo	as prepared	35.55 ± 31.85	60.03 ± 34.97	0.30 ± 0.36	1.69 ± 0.56	0.94 ± 1.20
	annealed	36.53 ± 25.20	44.75 ± 36.54	6.61 ± 9.19	5.35 ± 7.31	6.78 ± 9.47

This band may consist of overlapping contributions from Ni—O, Mn—O, and Co—O vibrations, indicating the formation of a structurally reorganized but still disordered mixed-metal oxide phase.

The NiMnFe sample showed the most pronounced band shifts among the series, with M—O bands shifting from ~250, ~450, and ~520 cm^{-1} in the as-prepared state to ~300, ~600, and ~670 cm^{-1} after annealing and are assigned to the Fe—O,[54] Ni—O, and Mn—O vibrations, respectively. Since XAS shows that Ni and Fe oxidation states remained largely unchanged, while Mn underwent significant oxidation, the increased intensity and shift of the higher-frequency band (~670 cm^{-1}) likely reflects a reorganization of the oxide network and the development of stronger Mn—O interactions within a more ordered structure as well as pointing toward a surface enrichment with oxidized Mn species after annealing, consistent with XPS results.

The annealed NiFeMo sample exhibited a distinct broad Raman feature in the 700–800 cm^{-1} region, consistent with Mo—O—M and Mo—O vibrations,[55] and lacked the sharp Mo═O terminal bond signals typically observed between 800–1000 cm^{-1},[56] indicating that Mo is incorporated in a disordered Mo—O bonding environment, rather than existing as isolated MoO_4^{2-} units. Several additional bands were observed around 180, 210, 270, 330, 370, 440, 510, and 550 cm^{-1}, which likely correspond to various M—O stretching and bending modes involving Mo, Fe, and Ni centers within the mixed oxide network. These modes are likely activated in this sample due to the larger atomic radius of Mo in comparison to Mn, which induces greater structural distortions and lowers symmetry.

2.2.5. Electrochemically Active Surface Area

The electrochemically active surface area (ECSA) of the fabricated samples was measured using the double-layer capacitance

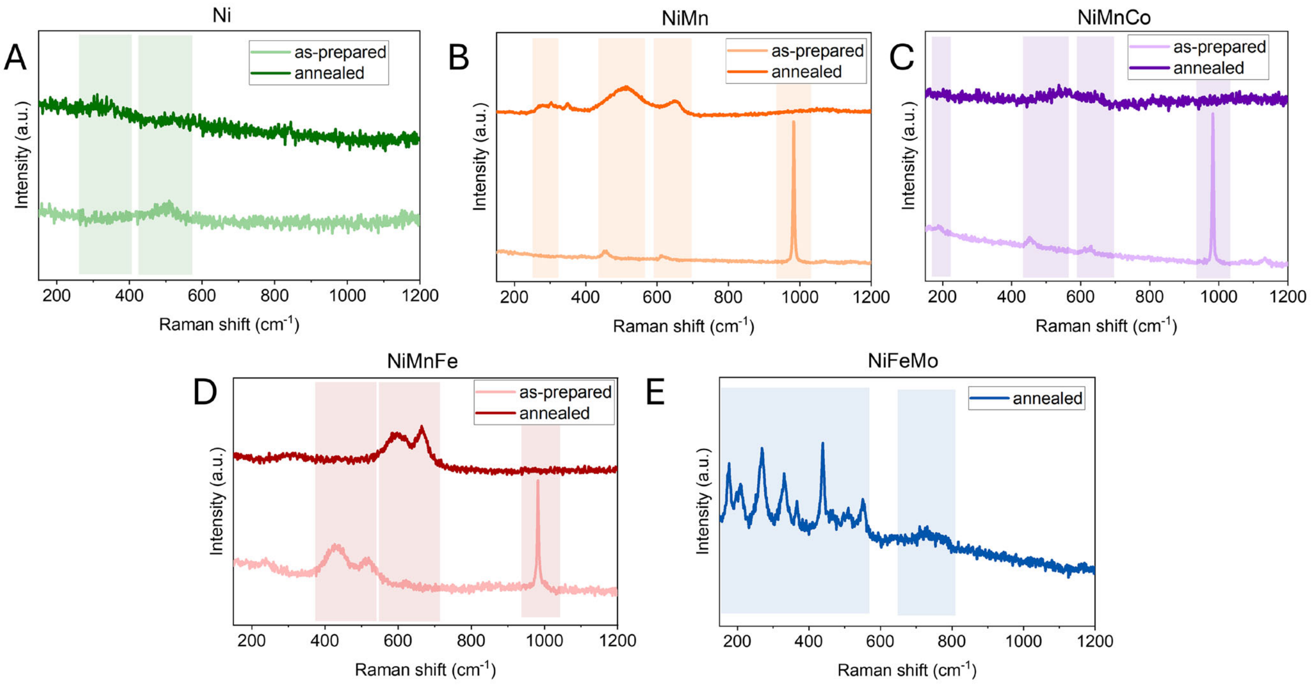

Figure 8. Raman spectra of foams fabricated for 20 min. A) Ni foams; B) NiMn foams; C) NiMnCo foams; D) NiMnFe foams; and E) NiFeMo foams.

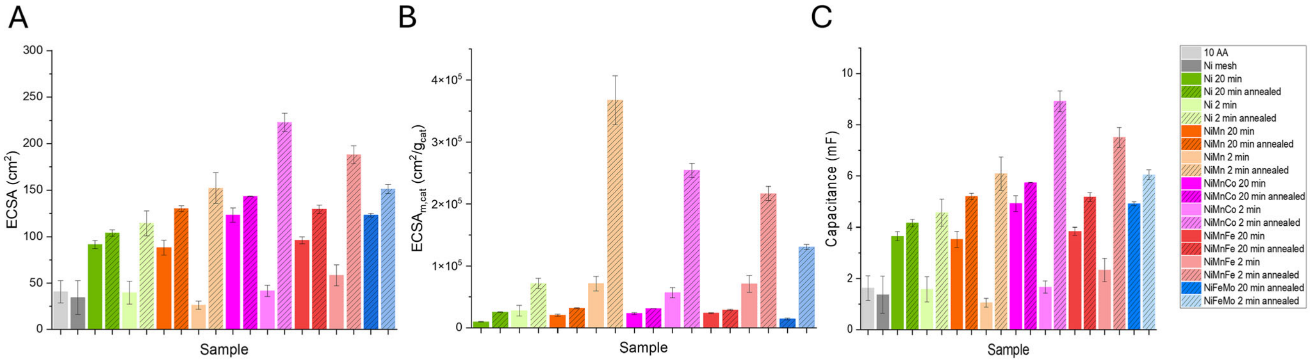

Figure 9. Measured ECSA (A), mass-normalized ECSA (B), and total capacitance of the tested samples (C).

method. **Figure 9** shows the ECSA, the mass-normalized ECSA ($ECSA_{g,\ cat}$) and the total capacitance of the tested samples.

As can be seen, both substrate materials (carbon paper and Ni mesh) possess the same and lowest ECSA, measuring just under 50 cm^2. Annealing increases the active surface area for all samples, with the effect being more pronounced in those electrodeposited for shorter durations (120 s). This is likely due to surface nanocrystallization, which is supported by the SEM measurement, where the surface of the samples appears more crystalline after the annealing treatment, a trend also suggested by the XAS results. This is in line with previous reports that highlight this nanocrystallization effect caused by annealing.[57–59]

Interestingly, before annealing the ECSA increases with deposition time, as would be expected, since more mass is deposited. However, upon annealing, the trend is reversed, and the ECSA becomes larger for samples that were deposited for shorter durations. This is particularly evident in the mass-normalized ECSA (Figure 9B).

In the case of the pure Ni samples this could be attributed to surface reorganization, as electrodeposited Ni has a highly amorphous character, which changes after annealing. The transition to a more crystalline structure leads to a rougher surface (see Figure 4C) due to grain grooving, a phenomenon observed in Ni thin films annealed at 700 °C, where Ni tends to diffuse away from the grain boundary region.[60]

In the Mn- and Mo-containing samples, this may originate from the segregation of Mn, Co, and Fe toward the surface during annealing, as shown by XPS results. As these atoms segregate toward the surface, they contribute to more grain boundaries thereby increasing the surface area. The less pronounced surface increase in Mo-containing samples might be due to Mo being a 4d transition metal, which forms stronger bonds with the host matrix compared to Mn (a 3d transition metal). Consequently, Mn is expected to diffuse more rapidly within the Ni/Fe matrix, resulting in greater Mn enrichment at the surface and a higher number of grain boundaries. Given that the ECSA determination could be somewhat inaccurate—due to the lack of a clear capacitive region of the samples and the assumption of a fixed specific capacitance of 40 µF cm^{-2}— reporting the measured capacitance (Figure 9C) may offer a more reliable comparison. However, it follows the same trend as the ECSA, for the same reasons.

Regarding $ECSA_{g,\ cat}$ (Figure 9B), this value is highest for all annealed samples, and particularly large for those deposited for only 2 min. The largest $ECSA_{g,\ cat}$ is found for the NiMn foam, followed by NiMnCo, NiMnFe, and NiFeMo foams, with values of 36, 25, and 22 m^2 g_{cat}^{-1}, respectively. This trend again likely results from Mn (and to a lesser extent Mo) atoms being larger than the Ni/Fe atoms and migrating toward the foam surface, as evidenced by XAS data. As the foams deposited for 2 min are thinner, it becomes much easier for the Mn/Mo atoms to reach the surface, generating structural defects that enhance the surface area.

It must be mentioned that, due to the macroporous nature of the pores, BET would not yield a reliable surface area for the samples containing micrometer-range pores.

2.3. Electrochemical Performance

The DHBT-prepared samples were evaluated for their electrocatalytic activity toward two model reactions: the OER and GOR. Pure Ni is chosen as the baseline for performance comparison in the subsequent set of experiments. Since the focus of this work is not on the performance toward a specific reaction, the discussion here centers on OER results, while GOR data are presented separately in Section S4 (Supporting Information).

2.3.1. Half-Cell Tests

All samples were first tested in the half-cell setup described in the Experimental Section. **Figure 10** shows the last OER CV cycle of all the tested samples, where all as-prepared samples (light-colored lines) show the characteristic Ni^{2+}/Ni^{3+} redox pair peaks at around 1.35 and 1.25 V (vs. RHE) in the anodic and cathodic sweeps, respectively. These peaks disappear once the samples are annealed (darker lines), indicating that Ni becomes redox inactive. Another interesting feature is the increase in the non-faradaic region of the CV ($\leqslant$ 1.0 V) becoming more pronounced upon annealing, which is an indication of the increased surface area that such samples possess and which has been confirmed through ECSA measurements. Additionally, the peak current density at 1.6 V decreases upon annealing (also shown in **Figure 11A**), indicating that a higher crystallinity of the sample is not necessarily correlated with higher OER activity, as has been previously demonstrated in other studies.[61,62]

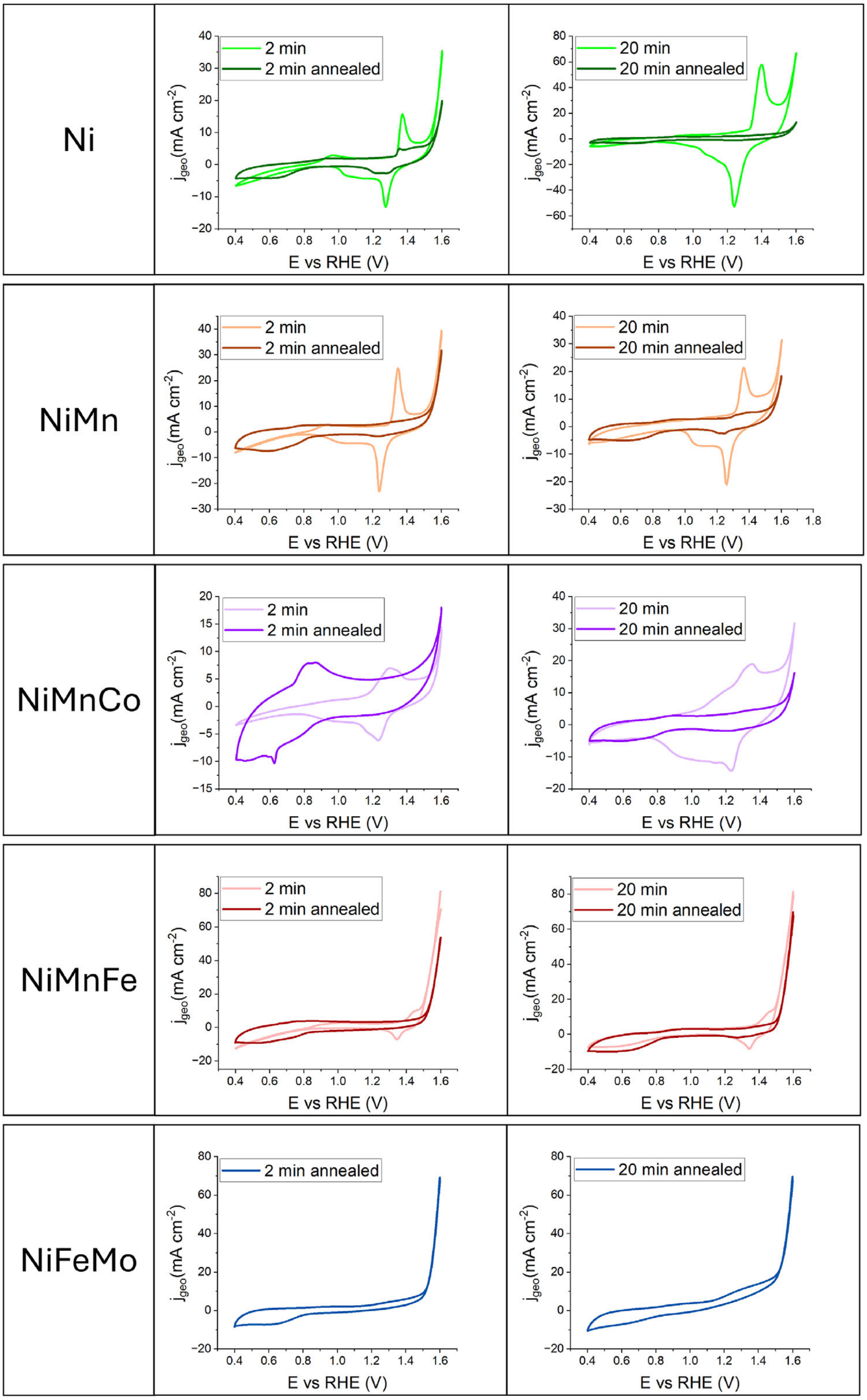

Figure 10. Representative CVs of the fabricated samples toward OER. The last CV cycle is shown for all samples. The left and right columns show the CVs for the samples electrodeposited for 2 and 20 min, respectively. CVs acquired from 0.4 to 1.6 V (vs. RHE) at 20 mV s^{-1}. Ten cycles were acquired and the last scan is shown.

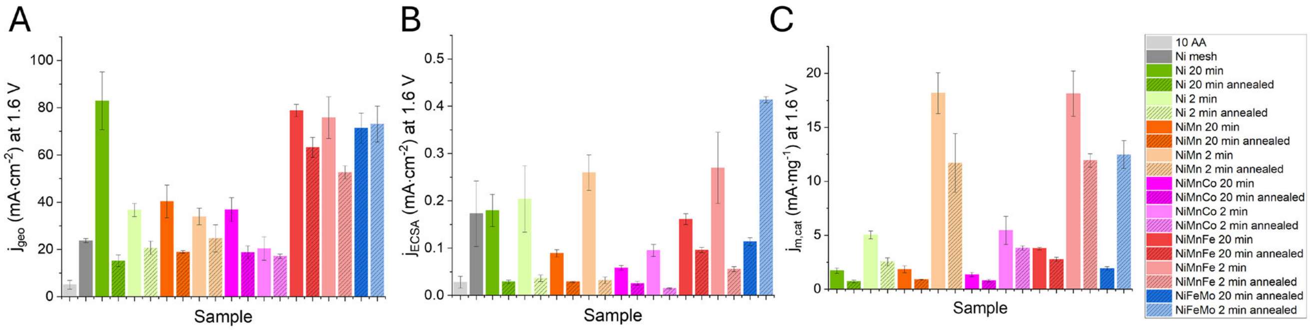

Figure 11. Calculated values (at 1.6V vs RHE) of current density (A), ECSA-normalized current density (B), and mass-normalized current density (C). Values are calculated at 1.6 V vs. RHE.

It would seem that the pure Ni foam (20 min deposition) is the best catalyst of the tested samples, if we limit ourselves to considering the geometric current density (j_{geo}) at 1.6 V (Figure 11A). In this case, Ni would be followed by the tri-metallic foams containing Fe (NiMnFe and NiFeMo), which reach around 80 mA cm^{-2}. When considering the ECSA, the current density (j_{ECSA} - Figure 11B) is highest for the thinner Mo-containing sample, followed by the thin (2 min deposition) and as-prepared samples. However, this metric also shows that the Ni mesh substrate performs at the same level as the pure Ni foams, with the thin and as-prepared NiMn and NiMnFe samples only slightly outperforming the substrate. It is when we normalize the current by the deposited catalyst mass ($j_{m,\,cat}$, shown in Figure 11C) that we find surprising results. In this case, the best performing samples are the thin (2 min deposition) NiMn and NiMnFe samples, with the as-prepared samples performing best and reaching up to 18 mA mg_{cat}^{-1}, followed by their annealed counterparts as well as the thin NiFeMo samples. Using this metric, the Ni samples rank near the bottom for performance toward OER. It is not surprising to have the NiMnFe sample as a top performer, since NiFe-based catalysts have been shown to perform well for OER.[63]

2.3.2. In Situ Raman Spectroscopy

In situ Raman spectroscopy was employed to monitor the structural evolution of selected Ni-based catalysts: NiMnFe for its high specific mass-activity, NiMnCo as a tri-metallic catalyst with poor OER performance, and the Ni sample, as a performance baseline.

As shown in **Figure 12**, the in situ Raman spectra reveal distinct potential-dependent transformations for each Ni-based catalyst. In the case of as-prepared NiMnFe, the initial spectrum at open circuit potential (OCV) displays broad features in the 400–600 cm^{-1} region, which evolve into a pronounced shoulder near 600 cm^{-1} starting at 1.2 V. This feature, commonly associated with disordered Ni—O species or partially oxidized transition metal oxides, disappears completely at 1.6 V, indicating a potential-induced surface reconstruction into a more ordered γ-NiOOH phase, which is known to be catalytically active for OER.[64] Notably, the γ-NiOOH signals in NiMnFe are significantly more intense than those observed in the other samples, suggesting a more extensive and efficient formation of the catalytically active phase. This likely contributes to the superior electrochemical performance of NiMnFe, both in terms of current density and mass-specific activity. Furthermore the γ-NiOOH bands appear when the applied potential is 1.4 V, correlating well with the Ni^{2+}/Ni^{3+} anodic peak at 1.35 V (Figure 10). Additionally, the presence of this phase is supported by the XRD results, which show the presence of the β-Ni(OH)$_2$ phase, a known precursor to γ-NiOOH under OER conditions.[65]

A similar evolution is observed for NiMnCo (as-prepared), though with notable differences. Here, the 600 cm^{-1} band appears earlier, at 1.0 V, and with greater intensity than in NiMnFe. This signal decreases in intensity around 1.3 V, transitioning into a broader shoulder that persists at higher potentials, suggesting a slower or less complete surface reorganization. Additionally, a band near 500–520 cm^{-1} at OCV — likely attributable to Ni(OH)$_2$ or an intermediate oxyhydroxide — shifts to approximately 470 cm^{-1}, consistent with the formation of γ-NiOOH. However, the broader and less-defined nature of these features, combined with the lower intensity of the NiOOH band, indicates a less efficient or incomplete phase transition. This may account for the lower mass-specific and geometric current density performance of NiMnCo compared to NiMnFe.

The as-prepared Ni sample exhibits similar Raman features to NiMnCo, including a persistent shoulder near 600 cm^{-1} and the evolution of a band near 470 cm^{-1} at higher potentials, corresponding to γ-NiOOH. Before 1.4 V, the spectra are dominated by a growing band in the 450–500 cm^{-1} region, attributed to Ni—O vibrations of Ni(OH)$_2$ or lower-valence Ni species. The γ-NiOOH band becomes clearly resolved only at 1.4 V and above, indicating delayed formation of the active phase. While the overall Raman intensity is lower, the features in the 400–600 cm^{-1} region are more distinctly separated, suggesting a relatively well-defined but less abundant γ-NiOOH phase. Despite achieving high geometric current densities, Ni shows lower mass-specific activity, likely due to high mass loading and limited utilization of electrochemically active sites, as supported by the weak Raman signal of the active phase.

In contrast, the annealed samples show markedly different behavior. For annealed Ni, the spectrum displays only weak and broad features in the 400–600 cm^{-1} region throughout the applied potential range. A faint band near 1050–1075 cm^{-1} is also observed, which disappears at 1.6 V. Although the exact origin of this feature remains unclear, it may relate to adsorbed oxygen intermediate such as OH^{-}.[66] Its disappearance at high potential supports the interpretation that it is not part of the OER-active phase. Overall, the absence of a clear γ-NiOOH transition and

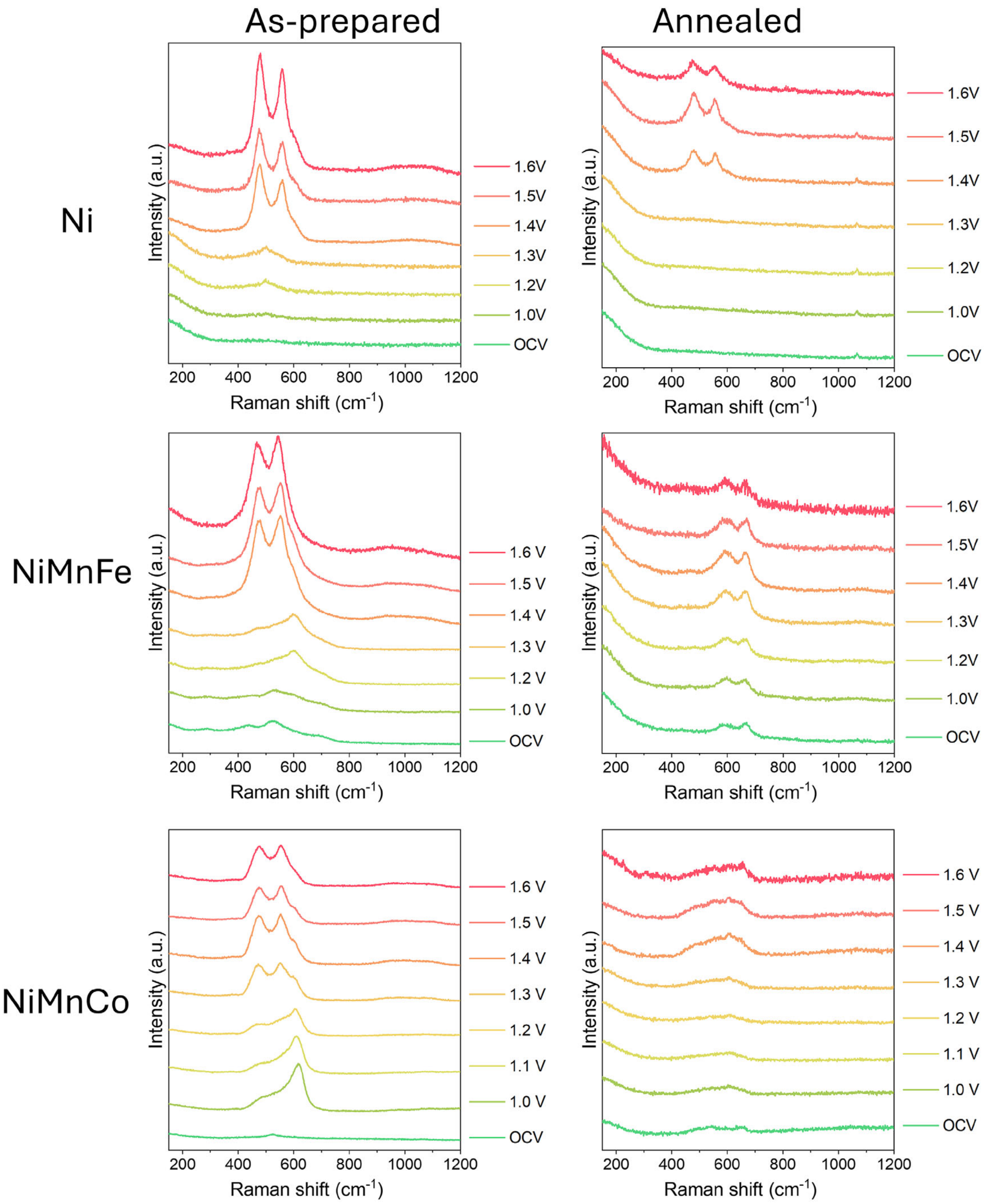

Figure 12. In situ Raman spectra taken of the Ni (top row), NiMnFe (middle row), and NiMnCo (bottom row).

weak spectral features align with the reduced catalytic activity of the annealed Ni sample.

For annealed NiMnFe, broad features in the 550–700 cm^{-1} region are already present at OCV and persist across the potential range. These signals are consistent with Ni(Fe/Mn) oxyhydroxide-type vibrations, indicating some degree of preformed oxidized species after thermal treatment. However, the bands remain broad and weak, suggesting a disordered or poorly crystalline phase that does not evolve under applied potential. This structural rigidity may limit the formation of well-defined γ-NiOOH, which could explain the significantly lower OER activity of annealed NiMnFe.

The annealed NiMnCo sample also displays very broad and unresolved features spanning 400–700 cm^{-1}, visible already at OCV. At early potentials, the spectrum appears to contain two overlapping bands, which merge into a single, broad and featureless signal from 1.0 to 1.3 V. At 1.4 V and above, two overlapping contributions again become discernible, but they remain poorly

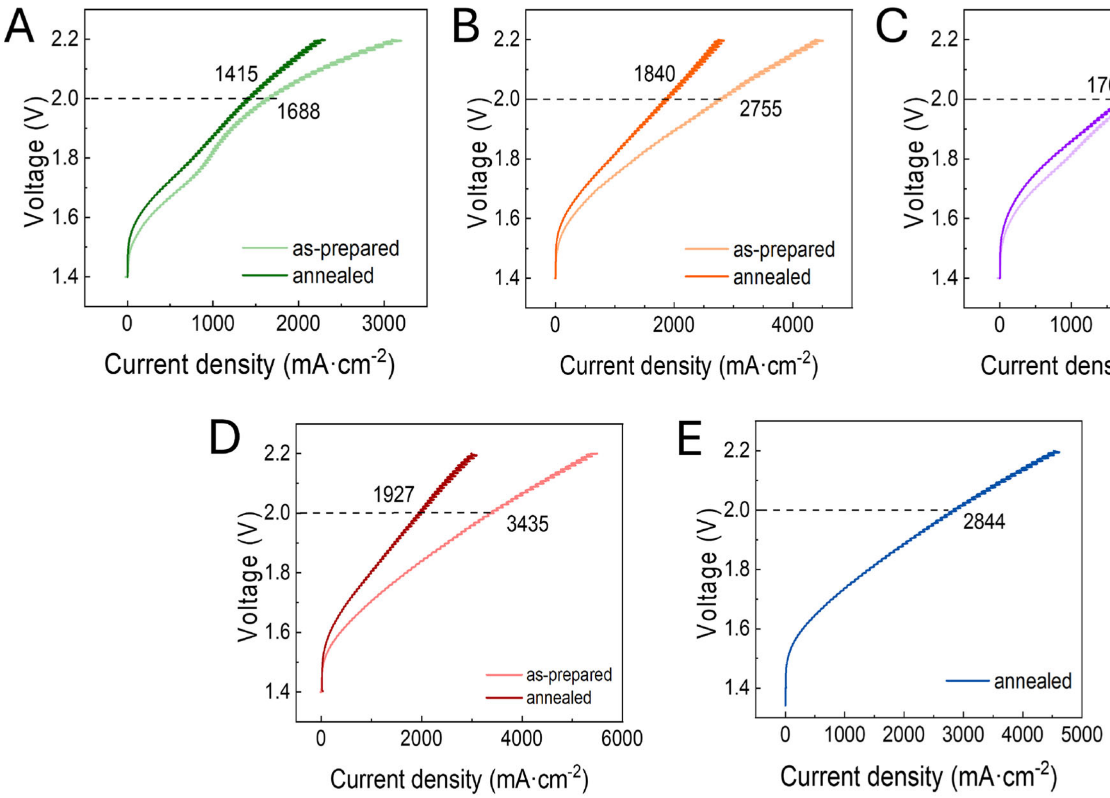

Figure 13. Voltage sweep curves of the Ni (A), NiMn (B), NiMnCo (C), NiMnFe (D), NiFeMo (E) foams. Measurements were performed in 1 mol L^{-1} KOH, at 60 °C. The marked numbers show the current density obtained at a cell voltage of 2.0 V.

resolved and low in intensity. This behavior indicates an ill-defined and dynamically disordered oxyhydroxide phase that fails to develop into a catalytically efficient γ-NiOOH structure. The lack of spectral sharpening and low intensity is consistent with the poor OER performance of annealed NiMnCo, both in terms of current density and mass-specific activity.

2.3.3. Anion Exchange Membrane Water Electrolysis Tests

The samples were additionally tested in an anion exchange membrane water electrolyzer (AEMWE), as described in the Experimental Section. The results are summarized in **Figure 13**. The AEMWE single-cell measurements reveal a clear trend in catalytic activity among the tested Ni-based electrodes. Notably, the as-prepared NiMnFe catalyst exhibited the highest performance, reaching a current density of over 3400 mA cm^{-2} at 2.0 V in 1 mol L^{-1} KOH at 60 °C. This value surpasses many comparable systems reported in the literature, even under more concentrated alkaline conditions or elevated temperatures, underscoring the excellent intrinsic activity of this composition.[66–68] As before, annealing consistently led to a reduction in performance here as well. NiFeMo, although slightly less active than NiMnFe, still achieved over 2800 mA cm^{-2} at 2.0 V. These findings highlight the importance of compositional tuning and the effect of thermal treatment in optimizing the DHBT-prepared electrocatalysts for AEMWE, with as-prepared multimetallic systems showing the most promising activity under realistic operational conditions.

Electrochemical impedance spectroscopy (EIS) was also employed to evaluate the electrode kinetics and interfacial properties. As shown in Figure S8, the as-prepared Ni-based catalysts generally exhibit significantly lower charge transfer resistance (R_{ct}) values compared to the annealed counterparts, indicating more efficient charge transfer from the electrode to the electrolyte, which is favorable for OER. Moreover, the ohmic resistance (R_{ohm}) of the as-prepared samples is also consistently lower, further confirming their superior interfacial conductivity and enhanced electrochemical performance.

3. Conclusion and Outlook

In summary, the DHBT method proved to be a facile and effective approach for preparing microstructured catalysts, provided that sufficiently high current densities ($|j| \geqslant 100$ mA cm^{-2}) are maintained during deposition. During the annealing process, significant surface redistribution of elements was observed. XPS indicates that Fe and Co become enriched at the surface, while Ni tends to be depleted, and Mn shows only a moderate increase in selected compositions. These trends suggest thermally driven segregation processes, likely influenced by differences in atomic size, surface energy, and alloying enthalpy. The associated restructuring may contribute to the observed increase in ECSA, potentially driven by grain boundary formation and nanocrystallization effects.

Among the samples, NiMn exhibited the highest post-annealing $ECSA_{g, cat}$ (36 m^2 g_{cat}^{-1}), followed by NiMnCo

Table 4. Chemical composition of the baths used for the DHBT procedures.

Chemical	Ni bath[a]	NiMn bath	NiMnCo bath	NiMnFe bath	NiFeMo bath
$NiSO_4$	50 mM	50 mM	50 mM	50 mM	50 mM
$MnSO_4$	–	50 mM	50 mM	50 mM	–
$CoSO_4$	–	–	50 mM	–	–
$FeSO_4$	–	–	–	50 mM	50 mM
$NaMoO_4$	–	–	–	–	5 mM
$(NH_4)_2SO_4$	2 M	1 M	0.8 M	0.8 M	0.8 M
Sodium citrate	–	–	10 mM	10 mM	10 mM

[a] The Ni bath used chlorides, rather than sulfates

($25\ m^2\ g_{cat}^{-1}$); however, this enhancement did not lead to improved oxygen evolution reaction (OER) performance. In contrast, NiMn and NiMnFe showed the highest mass-specific activities, with NiFeMo performing comparably. AEMWE tests further demonstrated the viability of these materials for OER, with NiMnFe achieving superior performance (j_{max} >3400 mA cm^{-2} at 2 V) compared to previously reported compositions.

These findings underscore both the versatility and the limitations of DHBT-derived materials, pointing toward future strategies for enhancing catalytic efficiency through electrolyte and compositional tuning. Notably, annealing promotes the formation of crystalline and homogeneous alloys, which appears detrimental for OER and GOR electrocatalysis due to the loss of the redox-active Ni(OH)/NiOOH pair.

The current electrolyte composition supports the synthesis of multi-metallic structures; however, further optimization—particularly via reduction of salt concentrations—may enable the fabrication of tetra-metallic and even true high-entropy alloy (HEA) systems. However, for practical applications, the durability of the foam electrocatalysts must be thoroughly evaluated and remains a topic to be explored.

4. Experimental Section

Chemicals and Solutions: Nickel (II) sulfate heptahydrate (purum p.a., crystallized, ⩾ 99.0% (KT)), manganese (II) sulfate monohydrate (ReagentPlus ⩾ 99.0%), cobalt (II) sulfate heptahydrate (ReagentPlus ⩾ 99.0%), sodium molybdate dihydrate (ACS reagent, ⩾ 99.0%), sodium citrate monobasic (BioXtra, anhydrous, ⩾ 99.5% (T)), D-(+)-Glucose (⩾ 99.5% (GC)), and sulfuric acid (Puriss. p.a., for determination of Hg, ACS Reagent, Reag. ISO, Reag. Ph. Eur., 95.0–97.0%) were all acquired from Sigma-Aldrich.

Potassium hydroxide (analytical reagent grade) was purchased from Fischer Scientific, iron (II) sulfate heptahydrate (⩾ 99.0%, p.a. ACS), and ammonium chloride (purity 99.5%) were purchased from Carl Roth GmbH, Nickel (II) chloride hexahydrate (purity ⩾99.7%) was acquired from abcr GmbH, and ammonium sulfate (99.5% for analytical purpose) was purchased from Grüssing GmbH.

For the DHBT procedure, solutions were prepared as shown in **Table 4**, with the pH being adjusted to 2 using concentrated sulfuric acid. The concentration of ammonium sulfate was reduced as the number of metals increases to minimize salt precipitation in the solution. For the oxygen evolution reaction tests, a 1 M KOH solution was used. For the glucose oxidation tests, the solutions were prepared on the same day as the electrochemical tests took place, and consisted of 1 M KOH and 10 mM glucose.

Regarding the DHBT baths, the choice for using the sulfates of the metals was done mostly because of the Fe foams, as using chlorides (which can be found to be used in literature) leads to a rapid formation of iron chloride as soon as the foam is removed from the DHBT solution, which renders the foam unusable. It was found that sodium citrate is essential for helping to keep the process from generating insoluble compounds that might contaminate the fabricated electrocatalyst. It was found that without it, insoluble matter starts building up near the counter electrode whenever the Mn salt is present, and citrate eliminates this issue.

DHBT procedure: DHBT was performed using a Gamry Reference 3000 potentiostat equipped with the Reference 30K booster. The procedure was performed on two types of substrates: Ni mesh (Bekaert 2Ni18-050) and carbon paper (Sigracet 10 AA). The carbon substrate was used to allow the catalyst layer to be investigated by XAS. The substrates were first cut into pieces 4×3.5 cm^2. Prior to the DHBT procedure, the Ni mesh substrates were sonicated, first in acetone (for 15 min) and then in 2 M HCl (for 60 s), after which the substrates were washed with Milli-Q water and finally dried at 60 °C. Carbon paper substrates were not treated prior to DHBT, but care was taken to handle them with gloves to avoid contaminating them.

The DHBT procedure was performed in a two-electrode setup, using around 180 mL of solution, with the relevant substrate being the working electrode and a Pt mesh (ALS platinum gauze electrode, 80 mesh, lead wire 54 mm) acting as counter electrode. The exposed area of the substrates was 9 cm^2, which was defined by using Kapton tape to glue the substrate to a steel support. The steel support itself was also covered in Kapton tape, with only a small strip at the top remaining free of tape to allow for electrical contact.

The foams were deposited at a constant current (–9 A or –1 A cm^{-2}), using pulsed electrodeposition where current flowed for 1s, and was zero for one more second (duty cycle = $\frac{t_{ON}}{t_{ON}+t_{OFF}}$ = 50%). This was done for a total time of 2 or 20 min (i.e., the current is ON for a total of 1 and 10 minutes, respectively). Active cooling was achieved by pumping cold water (T⩽ 10 °C) around the reactor vessel (when deposition was performed for 20 min), and stirring with a magnetic stir bar was used as well (900 rpm).

After completing the DHBT deposition, the samples were immersed and sonicated sequentially in Milli-Q water and ethanol, for 5 min in each. The first step was used to remove any excess chemicals from the surface, and the latter to remove water from the surface to prevent oxidation. With the exception of the NiFeMo foams, these steps were enough to prevent oxidation of the sample and allow the samples to be stored normally for up to a few days.

Annealing was performed after this cleaning step. For NiFeMo samples, annealing was always performed (as otherwise oxidation quickly destroys the sample). In any case, annealing was always performed in the same way using a Carbolite tube furnace (Model EST 12/300): first the samples were heated to 900 °C at a rate of 5 °C min^{-1} and the temperature was held for 15 hours. The ramp down was done at a rate of 1 °C min^{-1}. Nitrogen was constantly flushed at a rate of 12 L min^{-1} to prevent the carbon paper from combusting.

Half-Cell Tests: The electrochemical performance test of the DHBT-prepared samples was performed in triplicate. The measurements were performed using a half-cell with the fabricated samples as working electrode (cut into 5 mm diameter disks), a platinum wire as counter electrode, and a Gaskatel Hydroflex hydrogen reference electrode. A BioLogic VSP-300 potentiostat was used and the measurements were performed in three steps: The first step was meant to aquire the CVs in 1 mol L^{-1} KOH. 10 cycles were performed at a scan rate of 20 mV s^{-1} from 0.4 to 1.6 V (vs. RHE); the second step was used to determine the ECSA. The CVs for this step were performed within 50 mV of the OCV (from OCV-50 mV to OCV+50 mV) at scan rates ranging from 10 to 100 mV s^{-1}. The potential was held at each of the CV edges for 10 s to properly polarize the sample; the last step was the same as the first one, but was performed with the addition of 10 mmol L^{-1} glucose. All measurements were performed with 80% resistance compensation (measured with the current-interrupt method).

Anion Exchange Membrane Water Electrolysis tests: Single-cell AEMWE tests were conducted using a potentiostatic/galvanostatic workstation (Biologic BT-815, max. 15 A, 10 kHz). A 1 cm^2 cell equipped with full nickel serpentine flow fields on both electrodes was employed. To ensure leak-tight operation, PTFE gaskets were used. The AEM was a PiperION Anion Exchange Membrane, 40 microns thick. Both compartments were independently supplied with 1 mol L^{-1} KOH at a flow rate of 10 mL min^{-1}. The operating temperature was maintained at 60 °C, aligning with the optimal range for AEM-based systems, which are constrained by chemical instability at elevated temperatures. Prior to operation, the cell was assembled at room temperature using an anion exchange membrane that had been pre-soaked in the electrolyte for 3 h. The initial conditioning phase involved a voltage sweep from 1.4 to 2.2 V at a scan rate of 100 mV s^{-1} for 10 cycles. Subsequent polarization curves were recorded by a voltage sweep from 1.4 to 2.2 V at a scan rate of 5 mV s^{-1}. Electrochemical impedance spectroscopy (EIS) measurements were performed under steady-state conditions at current densities of 100, 300, and 1000 mA cm^{-2} to evaluate the cell's resistive behavior.

SEM/EDX Measurements: SEM/EDX measurements were performed using a Zeiss Ultra plus scanning electron microscope equipped with a Peltier cooled Ultra Dry EDS-detector (Thermo Fisher Scientific, 30 mm^2). For the pore size distribution the pore diameters of 35 pores from each sample were measured 3 times and the average and standard deviations were extracted.

XPS Measurements: XPS measurements were performed using the PHI 5000 VersaProbe III instrument equipped with a monochromatic Al Kα X-ray excitation source (1486.74 eV), with a beam diameter of 100 µm and a pass energy of 26 eV for survey scans and 224 eV for high-resolution scans. The surface structure was investigated for the Mn 2p3, Ni 2p3, Fe 2p3, Co 2p3, Mo 3d, and O 1s edges, and measurements were performed at two distinct points of each sample. Data analysis was carried out using CasaXPS software (Casa Software, Teignmouth, UK). Elemental quantification was performed by integrating the area under each high-resolution peak after Shirley background subtraction. The atomic percentages were calculated using the relative sensitivity factors (RSFs) provided by the CasaXPS library.

XRD Measurements: XRD measurements were performed with a Stoe, StadiMP diffractometer using a Mo K-alpha source. Measurements were performed in transmission mode while keeping the sample rotating.

Raman Spectroscopy Measurements: For ex-situ Raman spectroscopy, measurements were conducted using the LabRAM HR800 confocal Raman spectrometer with a 633 nm laser. Spectra were acquired with an acquisition time of 2 s per scan, accumulated over 30 scans. All measurements were performed in air at room temperature to analyze the structural properties of the catalysts before and after electrochemical testing.

In-situ electrochemical Raman spectroscopy was conducted using a LabRAM HR800 confocal Raman spectrometer, integrated with a SP 200 (BioLogic) potentiostat and a modified electrochemical Raman cell. A 633 nm laser was used as the excitation source, focused onto the sample surface via a dry objective (Olympus, 50×, NA = 0.5, WD = 10.6 mm). Potential-dependent Raman spectra were collected over 60 s (2 s per acquisition, repeated 30 times) after stabilizing each potential for 5 min in the range of 1.0 to 1.6 V vs RHE. The measurements were performed in duplicate

ICP-OES Measurements: ICP-OES measurements were performed using an Optima 7300 DV device from PerkinElmer. The device was equipped with a Meinhard nebulizer in an unbuffered cyclonic chamber. The measurements were performed with a power of 1300 W, with a plasma gas flow of 15 L min^{-1}, nebulizer gas flow of 0.6 L min^{-1}, auxiliary gas flow of 0.2 L min^{-1} and a pump rate of 1 mL min^{-1}. The axial analysis direction was used and the control software used was WinLab 32, version 5.3. The measurements were performed in triplicate.

Microwave Digestion: The samples were first prepared by microwave digestion using a Multiwave 3000 from Anton Paar. The samples were digested in an acid mixture containing 2 mL HNO_3 and 6 mL HCl. The digestion was performed by increasing the power to 1400 W (at a rate of 10 W min^{-1}, with 0 W kept for 15 min) and keeping it there for 60 min. Pressure was steadily increased to 60 bar (0.5 bar min^{-1}) and the temperature was 240 °C.

X-Ray Absorption Spectroscopy: The ex-situ XAS measurements were performed at the KMC-3 beamline at BESSY II (Berlin). The measurements were performed in transmission mode. Spectra at the Ni, Fe, Mn and Co K-edges were collected. The metallic foils were measured simultaneously with the samples and used to align the energy. The softwares Bessy_47b and SimXLite, both developed by the beam scientists at KMC-3 beamline (BESSY II – Berlin), were used for the data processing and EXAFS fitting, respectively. The ranges used for the EXAFS fit were: k = [3.0; 12.5] $Å^{-1}$ and R = [1.0; 5.0] Å for Ni K-edge, k = [3.0; 12.5] $Å^{-1}$ and R = [1.0; 3.0] Å for Fe K-edge, k = [3.0; 12.5] $Å^{-1}$ and R = [1.0; 3.5] Å for Mn K-edge, and k = [2.3; 12.5] $Å^{-1}$ and R = [1.0; 3.0] Å for Co K-edge. The metallic foils were used to determine the amplitude factor, S_0^2, that was equal to 0.85, 0.75, 0.75 and 0.9 for Ni, Fe, Mn and Co K-edges, respectively. The scattering paths were obtained using the FEFF8 software.

Statistical Analysis: All experimental data were visually inspected for completeness and consistency prior to statistical analysis. Minimal preprocessing was applied; in some cases, minor noise reduction was performed to improve signal clarity. In particular, XAS data were processed using standard procedures, including normalization and energy alignment, to ensure comparability across samples. No formal outlier removal or data transformations were conducted unless explicitly stated.

No formal hypothesis testing was performed. Instead, statistical differences between conditions were evaluated based on descriptive statistics, primarily by comparing means and their associated standard deviations (SD). This approach was used to assess trends and reproducibility across independently prepared samples. All data are presented as mean ± SD, with the sample size (n) provided in the corresponding sections of the Experimental Section.

All statistical analyses were conducted using OriginPro 2024 (OriginLab Corp., Northampton, MA, USA). Image processing and quantification were performed using ImageJ (National Institutes of Health, USA). Additional software used for specific experimental techniques is detailed in the respective subsections of the Experimental Section.

Supporting Information

Supporting Information is available from the Wiley Online Library or from the author.

Acknowledgements

C.M.S.L. and B.F.G. are co first authors and contributed equally to this work. C.M.S.L. and C.R. acknowledge the funding granted by the Deutsche Forschungsgemeinschaft (DFG, German Research Foundation) - DFG priority program SPP 2370 (RO 2454/26-1). B.F.G. and C.R. acknowledge the Federal Ministry of Education and Research (BMBF) under the funding codes Live XAS (Grant 05K22WC1), HighHy (Grant 03SF0689B). L.G.V. acknowledges the funding granted by the São Paulo Research Foundation, FAPESP, (grant numbers #2024/06899-0, #2023/06233-9).

C.M.S.L. and B.F.G. thank Bessy (Berlin, Germany), a member of the Helmholtz Association, for the provision of experimental facilities. Parts of this research were carried out at the KMC-3 beamline, and the authors thank M. Haumann for assistance in using the beamline. Beamtime was allocated for proposal 251-13231-ST-1.1-P.

The authors thank the KeyLab Electron and Optical Microscopy, the Bavarian Polymer Institute, and Lena Geiling for their assistance in performing the SEM/XPS measurements. The authors thank Birgit Brunner and the Chair of Chemical Engineering for their assistance in performing the ICP-OES measurements.

Conflict of Interest

The authors declare no conflict of interest.

Data Availability Statement

The data that support the findings of this study are available from the corresponding author upon reasonable request.

Keywords

AEMWE, DHBT, electrocatalyst fabrication, glucose oxidation, OER, trimetallic electrocatalysts

Received: April 15, 2025
Revised: June 16, 2025
Published online: October 9, 2025

[1] C. H. Bartholomew, R. J. Farrauto, L. Dorazio, *Introduction to Catalysis and Industrial Catalytic Processes*, John Wiley & Sons Inc., Hoboken, NJ, USA, **2016**.
[2] R. Maity, B. S. Birenheide, F. Breher, B. Sarkar, *ChemCatChem* **2021**, *13*, 2337.
[3] S. Wei, W. Liu, C. Yang, P. Bai, X. Kong, W. Sun, *Mater. Chem. Front.* **2023**, *7*, 4723.
[4] S. H. Gebre, M. G. Sendeku, *J. Energy Chem.* **2022**, *65*, 329.
[5] S. Yesmin, S. J. Abbas, S.-C. Ke, *Appl. Catal., B* **2022**, *316*, 121629.
[6] A. Oh, Y. J. Sa, H. Hwang, H. Baik, J. Kim, B. Kim, S. H. Joo, K. Lee, *Nanoscale* **2016**, *8*, 16379.
[7] M. Lokanathan, I. M. Patil, B. Kakade, *Int. J. Hydrogen Energy* **2018**, *43*, 8983.
[8] J.-W. Yeh, S.-K. Chen, S.-J. Lin, J.-Y. Gan, T.-S. Chin, T.-T. Shun, C.-H. Tsau, S.-Y. Chang, *Adv. Eng. Mater.* **2004**, *6*, 299.
[9] M. Li, F. Lin, S. Zhang, R. Zhao, L. Tao, L. Li, J. Li, L. Zeng, M. Luo, S. Guo, *Sci. Adv.* **2024**, *10*.
[10] J.-T. Ren, L. Chen, H.-Y. Wang, Z.-Y. Yuan, *Chem. Soc. Rev.* **2023**, *52*, 8319.
[11] L. Xia, B. F. Gomes, W. Jiang, D. Escalera-López, Y. Wang, Y. Hu, A. Y. Faid, K. Wang, T. Chen, K. Zhao, X. Zhang, Y. Zhou, R. Ram, B. Polesso, A. Buha, J. Su, C. M. S. Lobo, M. Haumann, R. Spatschek, S. Sunde, L. Gan, M. Huang, X. Zhou, C. Roth, W. Lehnert, S. Cherevko, L. Gan, F. P. García de Arquer, M. Shviro, *Nat. Mater.* **2025**, *24*, 753.
[12] G. Allaedini, S. M. Tasirin, P. Aminayi, *Chem. Pap.* **2016**, *70*, 231.
[13] B. A. T. Mehrabadi, S. Eskandari, U. Khan, R. D. White, J. R. Regalbuto, vol. *61*, *Advances in Catalysis*, Academic Press, **2017**, pp. 1–35.
[14] M. A. Ehsan, R. Batool, A. S. Hakeem, S. Ali, M. F. Nazar, Z. Ullah, *Int. J. Hydrogen Energy* **2025**, *98*, 772.
[15] P. Karfa, K. C. Majhi, R. Madhuri, in *Two-Dimensional Nanostructures for Biomedical Technology*, (Eds.: R. Khan, S. Barua), Elsevier, **2020**, pp. 35–71.
[16] P. Benzo, S. Combettes, C. Garcia, T. Hungria, B. Pécassou, M.-J. Casanove, *ACS Energy Lett.* **2020**, *20*, 4144.
[17] A. Makhlouf, in *Nanocoatings and Ultra-Thin Films*, Woodhead Publishing Series in Metals and Surface Engineering, (Eds.: A. S. H. Makhlouf, I. Tiginyanu), Woodhead Publishing, **2011**, pp. 3–23.
[18] A. H. Al-Hammadi, A. Alnehia, A. Al-Sharabi, H. Alnahari, A.-B. Al-Odayni, *Sci. Rep.* **2023**, *13*.
[19] M. Marciello, Y. Luengo, M. P. Morales, in *Nanoarchitectonics for Smart Delivery and Drug Targeting*, (Eds.: A. M. Holban, A. M. Grumezescu), William Andrew Publishing, **2016**, pp. 667–694.
[20] F. Qin, M. K. Alam, F. Robles-Hernandez, L. Yu, C. S., Z. Ren, Z. Wang, J. Bao, *ACS Energy Lett.* **2018**, *3*, 546.
[21] (Eds.: M. Schlesinger, M. Paunovic), *Modern Electroplating*, 5th ed. edition.
[22] S. Vesztergom, A. Dutta, M. Rahaman, K. Kiran, I. Z. Montiel, P. Broekmann, *ChemCatChem* **2021**, *13*, 1039.
[23] A. S. Danial, M. M. Saleh, S. A. Salih, M. I. Awad, *J. Power Sources* **2015**, *293*, 101.
[24] C. Lin, H. Li, P. Zhang, C. Deng, L. Meng, S. Zhow, Q. Wang, J. Wu, C. Liu, J. Tian, Y. Qian, *J. Electroanal. Chem.* **2020**, *861*, 113946.
[25] A. C. de Sá, L. L. Paim, N. R. Stradiotto, *Int. J. Electrochem. Sci.* **2017**, *9*, 7746.
[26] A. Böhme, J. C. Bui, A. Q. Fenwick, R. Bhide, C. N. Feltenberger, A. J. Welch, A. J. King, A. T. Bell, A. Z. Weber, S. Ardo, H. A. Atwater, *Energy Environ. Sci.* **2023**, *16*, 1783.
[27] J. C. Bui, W. W. Lees, L. M. Pant, I. V. Zenyuk, A. T. Bell, A. Z. Weber, *Chem. Rev.* **2022**, *122*, 11022.
[28] F. J. Humphreys, M. Hatherly, *Recrystallization and Related Annealing Phenomena*, Elsevier, **2004**.
[29] A. I. Frenkel, *Chem. Soc. Rev.* **2012**, *41*, 8163.
[30] H. Liao, A. Fisher, Z. J. Xu, *Small* **2015**, *11*, 3221.
[31] P. K. Routh, E. Redekop, S. Prodinger, J. E. S. van der Hoeven, K. R. G. Lim, J. Aizenberg, M. Nachtegaal, A. H. Clark, A. I. Frenkel, *Nat. Commun.* **2024**, *15*, 6736.
[32] T. Han, Y. Li, Y. Cao, I. Lee, X. Zhou, A. I. Frenkel, F. Zaera, *J. Chem. Phys.* **2022**, *157*, 234706.
[33] R. Winand, *Electrochim. Acta* **1994**, *39*, 1091.
[34] Y. Li, Y.-Y. Song, Y. C., X.-H. Xia, *Electrochem. Commun.* **2007**, *9*, 981.
[35] K. I. Popov, S. S. Djokic, N. D. Nikolic, V. Jovic, in *Morphology of Electrochemically and Chemically Deposited Metals*, Springer Nature, **2016**, pp. 171–203.
[36] B. J. Plowman, L. A. Jones, S. K. Bhargava, *ChemComm* **2015**, *51*, 4331.
[37] J. Wang, H. Shao, S. Ren, A. Hu, M. Li, *Coatings* **2021**, *539*, 148045.
[38] Y. Reda, R. Abdel-Karim, K. M. Zohdy, S. El-Raghy, *Ain Shams Eng. J.* **2022**, *13*, 101532.
[39] Y. Li, L. L., W. Li, L. Lu, L. Tian, Y. Liu, C. Su, W. Tian, *Coatings* **2024**, *14*, 957.
[40] L. Zhang, Z. Shi, Y. Lin, F. Chong, Y. Qi, *Front. Chem.* **2022**, *10*.
[41] A. J. Bard, L. R. Faulkner, *Electrochemical methods: fundamentals and applications*, 2 edition, John Wiley & Sons Inc., Hoboken, NJ, USA, **2000**.
[42] R. Syed, S. K. Ghosh, P. U. Sastry, G. Sharma, R. C. Hubli, J. K. Chakravartty, *Surf. Coat. Technol.* **2015**, *261*, 15.
[43] Y. Qu, W. Zhou, X. Miao, Y. Li, L. Jiang, K. Pan, G. Tian, Z. Ren, G. Wang, H. Fu, *Chemistry an Asian J.* **2013**, *8*, 3085.
[44] M. G. Görn, R. M. Bolanz, S. Parry, J. Göttlicher, R. Steininger, J. Majzlan, *Clays Clay Miner.* **2021**, *69*, 188.
[45] W. D. Callister Jr., *Materials Science and Engineering: an Introduction*, John Wiley & Sons Inc., 7 edition, Hoboken, NJ, USA, **2007**.
[46] A. Labidi, *Appl. Sci.* **2023**, *13*, 2797.
[47] K. Ben-Mabrouk, T. H. Kauffmann, H. Aroui, M. D. Fontana, *J. Raman Spectrosc.* **2013**, *44*, 1603.
[48] S.-H. Lee, H. M. Cheong, N.-G. Park, C. E. Tracy, A. Mascarenhas, D. Benson, S. K. Deb, *Solid State Ionics* **2001**, *140*, 135.

[49] P. Scheitenberger, S. Brimaud, M. Lindén, *Mater. Adv.* **2021**, *2*, 3940.
[50] J. Strunk, M. A. Bañares, I. E. Wachs, *Top. Catal.* **2017**, *60*, 1577.
[51] Y. Ye, L. Li, J. R. Smyth, Z. Wang, D. Liu, X. Wang, C. Wang, *Phys. Chem. Miner.* **2019**, *46*, 705.
[52] Y. Yan, Z. Zhang, S.-M. Bak, S. Yao, X. Hu, Z. Shadike, F. Do-Thanh, C.-L. Zhang, H. Chen, X. Lyu, K. Chen, Y. Zhu, P. Lu, X. Ouyang, J. Fu, S. Dai, *ACS Catal.* **2019**, *9*, 1923.
[53] J. Jelicka, P. Vitek, H. G. M. Edwards, M. D. Hargreaves, T. Capoun, *J. Raman Spectrosc.* **2009**, *40*, 1082.
[54] B. J. Saikia, G. Parthasarathy, R. R. Borah, R. Borthakur, *Int. J. Geosciences* **2016**, *7*, 873.
[55] Q. Zhang, X. Li, Q. Ma, Z. Q., H. Bai, W. Yi, J. Liu, J. Han, G. Xi, *Nat. Commun.* **2017**, *8*, 14903.
[56] M. Dieterle, PhD Thesis, *10.14279/depositonce-327*, **2001**.
[57] C. Fu, L. Xu, Z. Dan, F. Qin, A. Makino, H. Chang, N. Hara, *J. Alloys Compd.* **2017**, *726*.
[58] K. Takenaka, A. D. Setyawan, P. Sharma, N. Nishiyama, A. Makino, *J. Magn. Magn. Mater.* **2016**, *401*.
[59] P. Sharma, X. Zhang, Y. Zhang, A. Makino, *Scr. Mater.* **2015**, *95*.
[60] D. Amram, L. Klinger, N. Gazit, H. Gluska, E. Rabkin, *Acta Mater.* **2014**, *69*.
[61] G. Chen, W. Zhou, D. Guan, J. Sunarso, Y. Zhu, X. Hu, W. Zhang, Z. Shao, *Sci. Adv.* **2017**, *3*, 6e1603206.
[62] S. Ju, Y. Liu, M. Pei, S. Shuai, Z. Zhai, W. Yan, Y.-J. Wang, J. Zhang, *J. Colloid Interface Sci.* **2024**, *653*, 1704.
[63] F. Dionigi, Z. Zeng, I. Sinev, T. Merzdorf, S. Deshpande, M. B. Lopez, S. Kunze, I. Zegkinoglou, H. Sarodnik, D. Fan, A. Bergmann, J. Drnec, J. F. de Araujo, M. Fliech, D. Teschner, J. Zhu, W.-X. Li, J. Jeffrey Freeley, B. R. Cuenya, P. Strasser, *Nat. Commun.* **2020**, *11*, 2522.
[64] S. Chen, L. Ma, Z. Huang, G. Liang, C. Zhi, *Cell Rep. Phys. Sci.* **2022**, *3*, 100729.
[65] R. P. Putra, I. B. Rachman, H. Horino, I. I. Rzeznicka, *Catal. Today* **2022**, *397-399*, 308.
[66] W. Jiang, A. Y. Faid, B. F. Gomes, I. Galkina, L. Xia, C. M. S. Lobo, M. Desmau, P. Borowski, H. Hartmann, A. Maljusch, A. Besmehn, C. Roth, S. Sunde, W. Lehnert, M. Shviro, *Adv. Funct. Mater.* **2022**, *32*, 2203520.
[67] Q. Xu, L. Zhang, J. Zhang, J. Wang, Y. Hu, H. Jiang, C. Li, *EnergyChem* **2017**, *4*, 100087.
[68] N. Du, C. Roy, M. Turnbull, S. Thiele, C. Bock, *Chem. Rev.* **2017**, *122*, 11830.